

Rotational remanent magnetization as a magnetic mineral diagnostic tool at low rotation rates

Mark W Hounslow^{1,2}, Chong-Shern Horng³ and Vassil Karloukovski¹

¹Lancaster Environment Centre, Lancaster University, Lancaster LA1 4YQ, UK. E-mail: mark.w.hounslow@gmail.com; v.karloukovski@lancaster.ac.uk

²Earth, Ocean and Ecological Sciences, University of Liverpool, Jane Herdman Building, Liverpool L3 5DA, UK

³Institute of Earth Sciences, Academia Sinica, PO Box 1-55, Nankang, Taipei 11529, Taiwan, E-mail: cshorng@earth.sinica.edu.tw

Accepted 2022 August 16. Received 2022 August 15; in original form 2022 February 2

SUMMARY

Prior work on rotational remanent magnetization (RRM) and rotational anhysteretic remanent magnetization (ARM_{ROT}) has demonstrated promise for magnetic mineral identification in earth materials. One challenge has been to calibrate the measurements to magnetic mineral types and microstructural controls, since previous studies have used differing spin rates, alternating field (AF) intensities and decay times, which hinders a comparison of data sets. Using a RAPID magnetometer we show that the range of usable practical rotation rates is 0.25–3 Hz [rps] which allows a wide range of RRM and ARM_{ROT} characteristics to be utilized (at 100 mT AF field, 100 μ T bias field). Sets of magnetic mineral extracts from sediments, and well characterized rock samples that contain the key magnetic minerals magnetite, pyrrhotite and greigite are used for a calibration of the RRM- ARM_{ROT} behaviour. Detrital pyrrhotite and pyrrhotite-bearing phyllites have largely small positive effective field (B_g) values (up to 6 μ T), with differences in B_g and ARM_{ROT} ratios at 0.5 and 2.5 Hz [rps] allowing grain size discrimination. The positive B_g values, and changes in RRM and ARM_{ROT} with rotation rates allow distinction of pyrrhotite from magnetite and diagenetic greigite. Diagenetic greigite has B_g values of –83 to –109 μ T (at 0.5 Hz [rps]) and unusual RRM variation at low rotation rates caused by anisotropy affects. In contrast to previous work, based on crushed and sized natural magnetite at high spin rates, B_g for single domain magnetite from intact bacterial magnetofossils from Upper Cretaceous Chalk has some of the lowest B_g (0–1 μ T) and displays a steep decline in ARM_{ROT} with increasing rotation rates. A simple tool for particle size characterization of magnetite may be the ratio of ARM_{ROT} at spin rates 2.5 and 0.5 Hz [rps]. Stability of RRM is better studied using RRM acquisition with increasing AF field intensity, since static demagnetization imparts a nuisance gyroremanence along the field axis. Mineral microstructure, dislocations and particle interactions are likely additional effects on RRM behaviour that need more investigation.

Key words: Magnetic properties; Biogenic magnetic minerals; Environmental magnetism; Magnetic mineralogy and petrology; Marine magnetism and palaeomagnetism; Rock and mineral magnetism.

1 INTRODUCTION

Rotational remanent magnetization (RRM) is related to the mechanisms of gyroremanent magnetization (GRM) acquisition when samples are rotated in a decreasing intensity alternating magnetic field (Wilson & Lomax 1972; Stephenson 1980; Potter & Stephenson 1986; Madsen 2003). The RRM produced is either parallel or antiparallel to the rotation vector, and for magnetite may be preferentially acquired by single domain (SD) particles (Potter & Stephenson 1986). The fact that RRM is preferentially acquired in SD particles, or those with high magnetic stability makes it

particularly attractive for investigating palaeomagnetic signal carriers, jointly with anhysteretic remanent magnetization (ARM) properties.

It has been shown that for crushed magnetite, the intensity of RRM acquisition may also be related to particle size (Potter & Stephenson 1986), and for diagenetic greigite the magnitude of RRM is considerably enhanced compared to magnetite (Snowball 1997b). This difference provides a simple, diagnostic tool for identification of diagenetic greigite, but not necessarily bacterial magnetofossil-greigite (Snowball 1997a,b; Reinholdsson *et al.* 2013; Chen 2014). RRM has not been detected in haematite

(Wilson & Lomax 1972; Potter & Stephenson 1986) but appears to be acquired by pyrrhotite (Thomson 1990). Despite the apparent utility of RRM for mineral magnetic identification, it has been little used, which may be due to four reasons: (1) the lack of widespread ‘off the shelf’ equipment for RRM application, (2) the often-weak RRM generated in many earth materials, (3) in many prior studies high spin rates generating the RRM were not conducive to routine study of wet or poorly consolidated sediment sample and (4) limited understanding of the various kinds of intrinsic and external controls on RRM and GRM production (Madsen 2003, 2004), especially at low rotation rates.

This work first addresses some of the practical issues with generating, measuring and interpreting RRM at low rotation rates. We use measurements from the 2G Enterprises RAPID magnetometer (Kirschvink *et al.* 2008, hereafter called the RAPID), which has the ability for controllable sample rotation at low rotation rates, allowing routine automated RRM measurement on conventional samples. More than 20 RAPID magnetometers are currently installed worldwide, and therefore this could allow more widespread application of RRM behaviours for mineral magnetic identification. The RRM in many sediments is also weak, and the high sensitivity of SQUID magnetometers allow RRM to be measured in most samples. Prior commercial instrumentation (Stephenson & Molyneux 1987) tackled the weak RRM intensity issue by rotation at large frequencies (i.e. ~ 100 Hz), which increases the RRM intensity, but is not conducive to studying wet, fragile or imperfectly shaped samples.

Secondly, we explore the utility of routine mineral magnetic identification, by using RRM behaviours on natural samples of known magnetic composition. These measurements allow us to suggest possible ways to effectively identify magnetic mineralogy in samples of unknown composition.

2 QUANTIFICATION OF RRM

RRM magnetizations are acquired with an alternating magnetic field (AF) is applied normal to the rotation axis of a specimen (Fig. 1), since RRM’s are a special type of the GRM acquisition process (Madsen 2004). To standardize the quantification of RRM, Stephenson (1980) and Potter & Stephenson (1986) suggested the following:

(i) An RRM magnetization that is produced parallel to the rotation vector is signed as positive, and when opposite to the rotation vector, is signed as a negative RRM. We follow this convention (Fig. 1). Some studies have followed the opposite convention (Wilson & Lomax 1972; Stephenson 1976; Edwards 1982b; Noel 1988) and when discussing these studies, we use a conversion to the convention of Stephenson (1980).

(ii) The magnitude of the RRM is related to the abundance of magnetic phases, and usefully Potter & Stephenson (1986) introduced the B_g parameter which normalizes the RRM by the ARM acquired under the same AF field and rotation conditions as the RRM. This kind of ARM is here symbolized as ARM_{ROT} (Fig. 1). The DC bias field used to generate the ARM_{ROT} is parallel to the rotation axis, but the AF field generating the ARM is aligned 90° to the rotation axis and DC field axis (Fig. 1). More widely used conventional methods of generation of ARM use co-axial AF and DC field axes to produce ARM (here referred as ARM_z). For a few samples we also investigated the ARM acquired at zero rotation rate as a proxy for ARM_{ROT} (see Supporting Information Section 3.1) as used in some prior studies (Snowball 1997b). Rotation rates are here expressed in revolutions per second (SI unit Hz) widely indicated

as ‘rps’ in much prior work, and here symbolized as ω in Hz [rps] units.

B_g , the effective gyromagnetic field in micro-Tesla (Potter & Stephenson 1986) is defined as:

$$B_g = B_a \times RRM / ARM_{ROT}, \quad (1)$$

where B_a = DC field used in generating the ARM (usually around 50–150 μ T)

2.1 Key attributes of RRM

The magnitude of RRM is partly dependent on the rotation rate. When the rotation rate exceeds the frequency (in Hz) of the AF field (i.e. the *AF threshold*) most magnetic materials have a greatly enhanced RRM intensity. This issue has led in a strong focus on RRM studies at large rotation rates (Table 1). We refer to low spin rates, as below the AF-field threshold and high spin rates above this—hence the separation of existing RRM data sets into Tables 2 and 3.

Magnetite, maghemite and greigite have positive RRM above the AF threshold, and largely negative (but not entirely negative), and much reduced RRM below this threshold. Conversion of B_g values between high spin to low spin values is open to much uncertainty—Snowball (1997b) used a conversion factor of -0.08 for transforming a magnetite B_g from 108 to 5 Hz [rps]. The synthetic Mapico black magnetite (Potter & Stephenson 1986; Edwards & Desta 1989) has been used in both low and high spin studies suggesting an alternative conversion factor of *ca.* -0.027 between 108 Hz [rps] and 0.07 Hz [rps]. For diagenetic greigite a conversion factor for B_g of -0.14 ± 0.06 for rotation rates between 95 Hz [rps] to 2.5 Hz [rps] is possible with values in Tables 2 and 3.

Multidomain (MD) magnetite and haematite have no or little appreciable RRM (Wilson & Lomax 1972; Potter & Stephenson 1986; Snowball 1997b). This is exemplified by basalt sample D264-2a (Tables 1 and 3) studied by Edwards (1982a, b) and Edwards & Desta (1989). This behaviour of MD magnetite is a useful property of RRM, since it implies that SD grains can be studied in mixed SD-MD earth materials that would acquire appreciable MD-related magnetizations using other magnetic investigation methods.

B_g for maghemite (γ - Fe_2O_3) may be in part concentration dependent, with larger B_g values in samples with larger concentrations of γ - Fe_2O_3 (Madsen 2003). Synthetic γ - Fe_2O_3 has some of the largest $|B_g|$ values for Fe-oxides at both low and high spin rates, but natural γ - Fe_2O_3 has so far not been studied (Tables 2 and 3).

CrO_2 recording tape particles have negative RRM above the AF threshold, and a largely positive RRM below the threshold (Madsen 2003), both in the opposite sense to that of magnetite (Table 2). Although Snowball (1997b) measured negative RRM at 5 Hz [rps] (Table 3) and Madsen (2003) negative RRM at 25 Hz [rps].

Heated pyrrhotite (either monoclinic or hexagonal) appears to display positive RRM both below and above the AF threshold (Tables 2 and 3), with rapid changes of RRM intensity close to the AF threshold. Unheated pyrrhotite studied by Thomson (1990) displayed negative RRM at 3 Hz [rps].

At AF frequencies below the AF threshold, the frequency of the field used may have little impact on the changes of RRM with rotation rate, or at least at rotation rates up to 0.1 Hz [rps] investigated by Edwards (1980a). However, the impact of differences in AF frequency at rotation rates further towards the AF threshold has not been investigated experimentally. Indeed, some theory suggests the

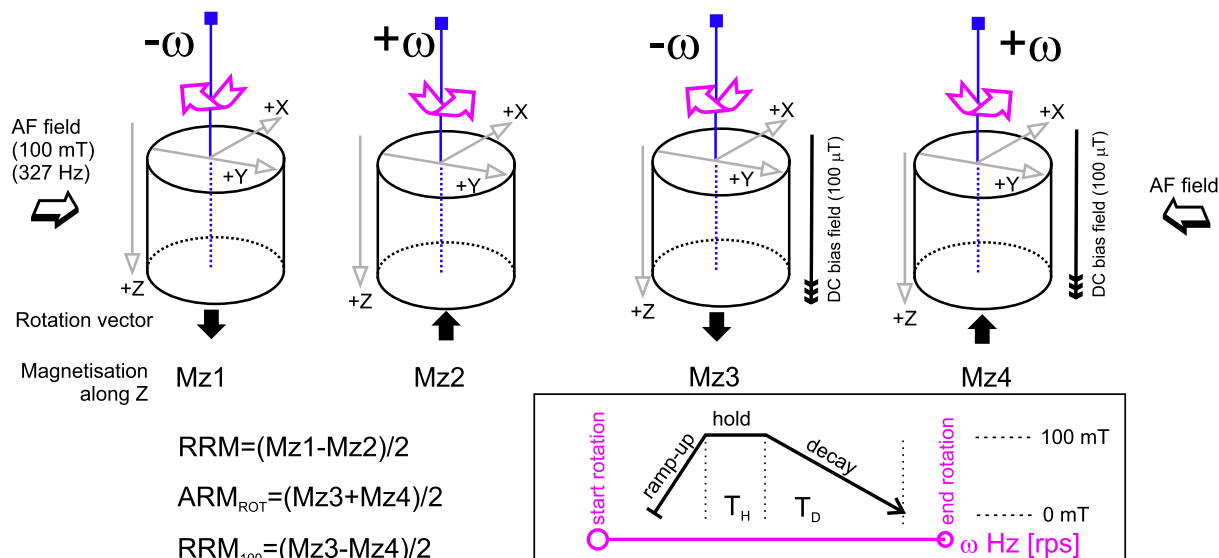


Figure 1. Schematic view of the rotational remanent magnetization (RRM) and rotational anhysteretic magnetization (ARM_{ROT}) measurement process. The rotation rate (ω) is symbolized also with a + or – sign indicating the down, or up-directed rotation vector. Inset shows the timing relationships between sample rotation and stages in the AF field build-up, hold and decay stages and their symbolized timings.

Table 1. Data sources for RRM and ARM_{ROT} versus rotation rates (ω in Hz [rps]). T_D , Alternating field decay time (i.e. demagnetizing field time) in seconds. ? = value unspecified. *Stephenson & Molyneux (1987) device uses decay rate of ~ 7 mT s^{-1} (hold time, $T_H = 5$ s), so this is assumed if not given in publication, when this device is used. TM, titanomagnetite.

Mineral/grain size	AF (Hz; mT)	ω range [T_D]	Ref. Fig.	Reference
Crushed magnetite <0.7 μ m	50;40,80	0–180 [~ 10]	fig. 6	Potter & Stephenson 1986
Natural magnetite 13–0.7 μ m	50;60	0–200 [~ 10]	fig. 5	Potter & Stephenson 1986
Mapico magnetite (0.2–0.8 μ m), Cubical	50;60	0–200 [~ 10]	fig. 5	Potter & Stephenson 1986
Synthetic magnetite	50;50–60	0.01–6 [?]	fig. 3	Wilson & Lomax 1972
2.2–4.4 magnetite	50;80	0–100 [11.4*]	fig. 2	Stephenson & Snowball 2001
Synthetic magnetite (63–125 μ m)	63.5,1210;40–55;	0.003–0.10 [45]	fig. 1	Edwards 1980a
Synthetic magnetite (63–125 μ m)	128;55	0.003–0.40 [6.6,67]	fig. 8	Edwards 1982a,1982b,,
γ Fe ₂ O ₃ TDK tape, Type D. elongate	50;60	0–200 [~ 10]	fig. 5	Potter & Stephenson 1986
γ Fe ₂ O ₃	50;60	0–200 [\sim minutes?]	fig. 3	Madsen 2003
CrO ₂	50;65,80,95	0–200 [\sim minutes?]	fig. 3	Madsen 2003
Heated pyrrhotite	50;80	0–130 [11.4*]	fig. 3	Thomson 1990
Various pyrrhotite bearing rocks	??	–20 to +20 [?]	fig. 4c	Slotznick <i>et al.</i> 2016
BAM8, BMR7 natural greigite	50;80	0–100 [11.4*]	figs 3 and 4	Stephenson & Snowball 2001
Igneous rock sample A66B1	50;51	0–250 [few seconds]	figs 4 and 5	Stephenson 1980
Icelandic basalts C10-2a, S2-1a	50;80	0.01–60 [?]	fig. 5	Stephenson 1976
Igneous samples (TM bearing)	50;50–60	0.01–6 [?]	fig. 3	Wilson & Lomax 1972
Rock sample R1	63.5,1210;55	0.003–0.16 [45]	fig. 2	Edwards 1980a
Rock R1, Igneous samples F37B-1a, D264-26 (TM bearing)	128;55	0.003–0.4 [6.6,34,67 101]	figs 5, 6 and 7	Edwards 1982b, samples from Wilson & Lomax

ratio of the rotation rate and AF frequency should in part control the strength of RRM acquisition (Stephenson 1980, 1985)

At low rotation rates the time of decay of the AF field (T_D in seconds; Fig. 1) has a large impact on the changes of RRM with ω (Edwards 1982b), such that changes in RRM properties are best compared when expressed with respect to ωT_D (in revolutions) rather than using ω .

RRM acquisition is not an instantaneous process, some *ca.* 90° (or larger) of sample rotation at peak AF field is required for RRM to be fully acquired (Edwards 1982b; Roperch & Taylor 1986). In much demagnetization equipment this is impacted by the AF peak field hold time (T_H), which ideally should be long enough for this rotation ‘initialization’ to be achieved.

An RRM induced by a particular AF field may require a larger static demagnetizing AF field to fully demagnetize the induced RRM (Edwards 1980b). This effect is likely related to the angular dependency of the switching field (Madsen 2004). Like demagnetizing ARM or IRM (Stephenson 1983) the intensity-decay curve produced during demagnetization may differ between static or tumbling demagnetization methods.

Whilst some is understood about the general RRM behaviour of common magnetic material in earth materials, the wide range of rotation rates, AF and DC fields used in previous studies (Tables 2 and 3) and the hold and decay rates of the AF inducing field, hinders a general and detailed comparison of the mineral magnetic behaviours.

Table 2. RRM and Bg values measured at spin rates exceeding the AF frequency threshold. Rotation rate, ω , in Hz [rps]. [&] also gives data for AF field down to 20 mT, at approximately linear decrease for all, except for γ Fe₂O₃ TDK tape. * in 10⁻³ A m⁻¹, ** in 10⁻⁶ A m⁻¹. Negative RRM indicates RRM acquired opposite to the rotation vector (Fig. 1). \pm shows SD or uncertainty on Bg averages. Stephenson & Molyneux (1987) device uses decay rate ~ 7 mT s⁻¹ (5 s hold time), so this is assumed if not given in the publication using this machine. T_D, alternating field decay time (i.e. demagnetizing field) in seconds. ? = decay time unspecified, mins=unspecified minutes. ^CChen (2014) inconsistently uses sign on RRM, assume Bg has the correct sign. TM, titanomagnetite.

Mineral/grain size	AF (Hz, mT)	ω [T _D], DC Field (μ T)	Bg (μ T)	RRM, ARM _{ROT} ($\times 10^{-3}$ Am ² kg ⁻¹)	Reference
Crushed magnetite < 0.7 μ m	50,80	108 [\sim 10], 43	108 ^{&}	95,	Potter & Stephenson 1986
Crushed magnetite 0.7–2.2 μ m	50,80	108 [\sim 10], 43	44 ^{&}	33,	Potter & Stephenson 1986
Mapico magnetite (0.2–0.8 μ m), Cubical	50,80	108 [\sim 10], 43	301 ^{&}	177,	Potter & Stephenson 1986
Crushed magnetite 2.2–4.4 μ m	50,80	108 [\sim 10], 43	28 ^{&}	15.5,	Potter & Stephenson 1986
Crushed magnetite 2.2–4.4 μ m	50,80	95 [11.4*], 70	28	10.9, 39	Stephenson & Snowball 2001
Crushed magnetite 4.4–7.6 μ m	50,80	108 [\sim 10], 43	17.8 ^{&}	9.2,	Potter & Stephenson 1986
Crushed magnetite 7.6–13.1 μ m	50,80	108 [\sim 10], 43	8 ^{&}	2.9,	Potter & Stephenson 1986
Crushed magnetite 13.1–25.5 μ m	50,80	108 [\sim 10], 43	4.1 ^{&}	1.01,	Potter & Stephenson 1986
SD3 Crushed magnetite	50,95	90 [mins], 150	330	6.8, 18.3*	Madsen 2004
γ Fe ₂ O ₃ TDK tape, Type D. elongate	50,80	108 [\sim 10], 43	161 ^{&}	330,	Potter & Stephenson 1986
γ Fe ₂ O ₃ , BASF FT26 tape	50,95	90 [mins], 43	85 to 150	167 218	Madsen 2003, 2004
CrO ₂ , BASF CK40-13 tape	50,95	63 [mins], 70	–15	83.5, 7098	Madsen, 2003, 2004
Natural SD magnetite magnetosomes (water column)	50,80	95[11.4], 70	0	0,–	Chen 2014 ^C
MV-1 magnetite magnetosomes	50,80	95[11.4], 70	1, 10.9	0.105, 0.674**	Chen 2014 ^C
SD magnetite and greigite	50,80	95[11.4], 70	2.4, 5.6	0.037, 0.461	Chen 2014 ^C
SD greigite magnetosomes	50,80	95[11.4], 70	7.3, 22.5	0.0006, 0.00187	Chen 2014 ^C
Heated (315 °C) vein pyrrhotite	50,80	100[11.4–86.4], 70	–	3.3,–	Thomson 1990
Rock and pottery samples below					
DG1 vesicular basalt, Low Ti-TM	50,95	90 [mins], 150	34	1552, 1910*	Madsen 2004
DG17 vesicular basalt, Low Ti-TM	50,95	90 [mins], 150	26	1014, 2384*	Madsen 2004
T97A flood basalt with TM	50,95	65 [mins], 150	9	327.7, 5141*	Madsen 2004
T54A sill, with magnetite	50,95	70 [mins], 150	38	1368, 5824*	Madsen 2004
TC05, TM10, SD TM, Tiva Canyon Tuff	50,80	95[11.4], 70	32	0.804, 1.76	Chen 2014 ^C
Supska potsherd	50,80	95[11.4], 70	162	–,–	Mahon & Stephenson 1997
Soba potsherds	50,80	95[11.4], 70	82 \pm 16	–,–	Mahon & Stephenson 1997
Baranda potsherds	50,80	95[11.4], 70	23	–,–	Mahon & Stephenson 1997
YB7 marine sediment, maghemite	50,95	90 [mins], 150	89	26.7, 41.9*	Madsen 2004
Greigite bearing lake sediments	50,80	95 [11.4], 70	482 \pm 221	264, 33.1*	Hu <i>et al.</i> 2002
BAM8 natural greigite	50,80	95 [11.4*], 70	1050	998, 95	Stephenson & Snowball 2001
BMR7 natural greigite	50,80	95 [11.4*], 70	1070	375, 35	Stephenson & Snowball 2001
SD greigite, Gutingkeng Fm (EJC49.1c, EJC50.1c)	50,80	95[11.4], 70	552–790	0.201, 0.021	Chen 2014 ^C

This work focusses on five aspects of RRM behaviour at rotation rates ≤ 3 Hz [rps]: (1) the variation of RRM, ARM_{ROT} and Bg with rotation rate, (2) the magnitude and sign of Bg and RRM and (3) the stability of the RRM as measured by the median destructive field (MDF)—since MDF of the RRM has been shown to be a useful additional parameter in characterizing particle size and mineralogy (Potter & Stephenson 1986; Snowball 1997b); (4) the impact of differences in peak AF hold times (T_H) and (5) exploration of how RRM data sets could be used for magnetic mineral identification at $\omega T_D \leq 4.5$ revolutions.

3 MINERALOGY OF TEST SAMPLES

The sample sets used here comprise two types, magnetic concentrates (extracts) and natural rock samples of known magnetic mineralogy. These sample sets comprise:

Detrital monoclinic pyrrhotite from river sediment, collected in the upper reaches of the mountainous Zhoushui River (at 23.786836°N, 121.01097°E, Taiwan), which is sourced from the pyrrhotite-bearing metamorphic terranes in the Central Range (Horng *et al.* 2012). Pyrrhotite grains in sediments were extracted using a rare earth magnet and were purified magnetically several

times. The purified sample was then subdivided into five micro-sized fractions (<5, 5–10, 10–20, 20–38 and 38–63 μ m, samples PY1 to PY 5, respectively; Table 4; Fig. 2a) with sieves and membrane filters. XRD analyses determined their purities (Fig. S1). The larger detrital particle sizes show some minor evidence of oxidation to lepidocrocite and goethite (Supplementary Information Fig. S1).

Magnetic extracts using the method of Hounslow & Maher (1996, 1999). The magnetic extracts broadly represent two groups, those from sediments with intact or near-intact magnetic oxide assemblage (e.g. like Franke *et al.* 2007), and a set with residual discrete Fe-oxide components (and Fe-oxides inclusions in silicates) after early sulphidic diagenesis or deep-burial diagenesis (e.g. Hounslow *et al.* 1995; Hounslow 1996; Maher & Hallam 2005; Table 4). The extracts are from: (a) the late Triassic Lunde Formation (LU codes) from the North Sea, containing a residual suite of silt to sand-sized magnetic minerals after extensive diagenetic dissolution, with in some cases minor discrete magnetic oxides, but abundant Fe-oxide inclusions in associated silicates (Hounslow *et al.* 1995). (b) Quaternary and Pliocene sediments from the Owen Ridge (OR sample codes) and Madingley Rise (codes MR; on the Mascarene Plateau) both in the Indian Ocean. The Indian Ocean samples have detrital sources exclusively of well mixed, far travelled aeolian origin (Table 4). Some of these extracts also represent residual magnetic

Table 3. RRM and B_g values measured at spin rates below the AF frequency threshold. Rotation rate, ω , in Hz [rps]. ^{AR} = partial rotational ARM (static sample during AF decay). ^S = static ARM (parallel to spin axis, symbolised here as ARM_z) used to determine B_g. See caption to Table 2 for details.

Mineral/grain size	AF (Hz, mT)	ω [T _D], DC Field (μ T)	B _g (μ T)	RRM, ARM _{ROT} ($\times 10^{-3}$ Am ² kg ⁻¹)	Reference
γ Fe ₂ O ₃ Sony MC30	50,100	5 [?], 100	-5.5 ^S	-, -	Snowball 1997b
γ Fe ₂ O ₃ TDKD1	50,100	5 [?], 100	-8.0 ^S	-, -	Snowball 1997b
γ Fe ₂ O ₃ TDKD2	50,100	5 [?], 100	-7.1 ^S	-, -	Snowball 1997b
MCF0-1, Co- γ Fe ₂ O ₃	128,46	0.07 [15], 60	-37	-, 12 ^{AR}	Edwards & Desta 1989
GFO-1, γ Fe ₂ O ₃	128,46	0.07 [15], 60	-30	-, 31 ^{AR}	Edwards & Desta 1989
MBL-1, Mapico Black magnetite	128,46	0.07 [15], 60	-8	-, 9.7 ^{AR}	Edwards & Desta 1989
Magnetite (63–125 μ m), Mag6	128,18.4	0.4 [17], 60	3	-, 2.13 ^{AR}	Edwards & Desta 1989
MDM- MD detrital magnetite	50,100	5 [?], 100	0 ^{-S}	-, -	Snowball 1997b
CRO-1 CrO ₂ powder	128,46	0.07 [15], 60	-5	-, 2.0 ^{AR}	Edwards & Desta 1989
CrO ₂ TDKMF1	50,100	5 [?], 100	-31 ^S	-, -	Snowball 1997b
Rock R1-a	128,36.4	0.4 [17], 45	-15	-, 0.21 ^{AR}	Edwards & Desta 1989
D264-2a (TM bearing)	128,36.4	0.4 [17], 60	0	-, 0.12 ^{AR}	Edwards & Desta 1989
Carboniferous Lavas	800,150	1 [30], 15	-3.1 \pm 1.9 ^S	-260, 1350*	Roperch & Taylor 1986
Miocene Basalt (with -RRM)	800,150	1 [30], 15	-13.6 \pm 16.7 ^S	-1200, 1850*	Roperch & Taylor 1986
Miocene Basalt (with + RRM)	800,150	1 [30], 15	8.9 \pm 1.2 ^S	1120, 1910*	Roperch & Taylor 1986
Pliocene Basalt	800,150	1 [30], 15	-5.6 \pm 1.2 ^S	-290 780*	Roperch & Taylor 1986
Serpentine	800,150	1 [30], 15	-3.8 \pm 4.8 ^S	-50 200*	Roperch & Taylor 1986
Pajep8- SD magnetite	50,100	5 [52?], 100	-0.14 ^S	-, -	Snowball 1997b
magnetofossils + detrital					
Hol81- SD detrital magnetite	50,100	5 [52?], 100	14 ^S	-, -	Snowball 1997b
Hol252- SD detrital magnetite	50,100	5 [52?], 100	-3.6 ^S	-, -	Snowball 1997b
Embmr1-SD greigite sediment	50,100	5 [52?], 100	98 ^S	-, -	Snowball 1997b
Embmr5-SD greigite sediment	50,100	5 [52?], 100	-110 ^S	-, -	Snowball 1997b
Embmr6-SD greigite sediment	50,100	5 [52?], 100	84 ^S	-, -	Snowball 1997b
Embmr8-SD greigite sediment	50,100	5 [52?], 100	-101 ^S	-, -	Snowball 1997b
Bmr9x-SD greigite concentrate	50,100	5 [52?], 100	-108 ^S	-, -	Snowball 1997b
St15-SD greigite sediment	50,100	5 [52?], 100	-119 ^S	-, -	Snowball 1997b
St79x-SD greigite concentrate	50,100	5 [52?], 100	-137 ^S	-, -	Snowball 1997b
Heated (315 °C) pyrrhotite	50,80	~5 [11.4–86.4], 70	-	1.9, -	Thomson 1990

assemblages (Table 4). Extract samples with codes LU, OR and MR1 to MR3 are generally poor in fine-grained magnetic particles and represent the magnetic detrital fraction mostly $>2 \mu\text{m}$ in size (i.e. the E_{MP} extract type of Hounslow & Maher 1999). Samples MR4 to MR6 are E_{MPT} type extracts of Hounslow & Maher (1999) and contain largely detrital grains $<2 \mu\text{m}$ in size and in some cases contain accessory magnetite magnetofossils (i.e. MR4 and MR5). The E_{MPT} extracts may contain the bulk of the discrete-grain SD-sized particles. This is not to say that the E_{MP} extracts contain no SD-like magnetic grains, since these may be within the larger detrital grains. The E_{MP} extracts contain variable amounts of Fe-oxides as inclusions in silicates, reflected in the variable content of silicates in the extracts (see Supporting Information for details). Therefore, these extracts are representative of the key magnetic components often found in sediments of various ages, and those residual magnetic minerals elevated in relative abundance during diagenetic-related Fe-oxide dissolution (Roberts 2015).

Monoclinic pyrrhotite bearing phyllites (samples PY6 to PY9) from Taiwan (Fig. 2b) with relatively coarse grain size. Hysteresis data indicate B_{cr}/B_c of 1.10–1.12 and M_{rs}/M_s of 0.66–0.72 for these samples (Table S1). These are typical values for metamorphic pyrrhotite and are not necessarily indicative of SD properties (Hornig 2018).

Greigite samples from Plio-Pleistocene greigite-containing mudstones from the Lower Gutingkeng Formation, SW Taiwan (Hornig *et al.* 1998; Jiang *et al.* 2001; sample codes GR1 to GR4; Table 4). Hysteresis data indicate B_{cr}/B_c of 1.26–1.39 and M_{rs}/M_s of 0.54–0.63 for these samples (Table S1). Chen (2014) also measured the RRM in two samples from this location at high-spin rates (Table 2).

The diagenetic greigite in these samples is very fine-grained and widely dispersed through the phyllosilicate matrix (Fig. 2c).

Whole rock samples of the Upper Cretaceous Chalk (CC code samples), from southern England. These are from the stratigraphic level of sample CW9b originally figured by Montgomery *et al.* (1998) which contains abundant chains of prismatic magnetofossils (Fig. 2d) in extracts. These are also figured in Hounslow & Maher (1999) and Kopp & Kirschvink (2008) (Table 4). The magnetofossil chains in the extracts seem to reflect *in situ* preservation, since other extracts from the Chalk from elsewhere (unpublished data of Hounslow) do not show such high abundance of intact chains (Fig. 2d). These samples also contain an associated assemblage of Fe-oxides as inclusions in detrital quartz and feldspars but have very little detrital Fe-oxides outside silicate hosts (see Supporting Information for details).

Relatively unaltered fine-grained dolerites (SVD code) with a content of typical titanomagnetite, which has undergone high temperature alteration to ilmenite-magnetite intergrowths (Table 4), with margins altered to maghemite. Clots of magnetite and acicular rods of Fe-oxide occur in the groundmass (Gayer *et al.* 1966; Krumsiek *et al.* 1968; Halvorsen 1973). Some of the prior work using low rotation rate RRM was performed on similar basaltic rocks (Tables 1 and 3).

Samples of siltstones and sandstone from the De Geerdalen Formation from several locations in Svalbard (Table 4), which have a rather similar detrital magnetite magnetic mineralogy throughout (Hounslow *et al.* 2007, 2022). The succession has been subjected to complex diagenetic changes (Mørk 2013; Haile *et al.* 2018), which will have removed much of the original discrete Fe-oxides.

Table 4. The test samples used in this work. SD, single domain; MD, multidomain. T_c , Curie temperature; TM, titanomagnetite, Ti content (wt per cent). See the Supporting Information for further details about these test samples.

Sample codes	Description	Mineralogy	References
PY1	<5 μm magnetic separate from river sediment, Taiwan	Monoclinic pyrrhotite	Horng & Roberts 2006.
PY2	5–10 μm magnetic separate from river sediment, Taiwan	Monoclinic pyrrhotite cncon	Horng & Roberts 2006.
PY3	10–20 μm magnetic separate from river sediment, Taiwan	Monoclinic pyrrhotite	Horng & Roberts 2006.
PY4	20–38 μm magnetic separate from river sediment, Taiwan	Monoclinic pyrrhotite, quartz, goethite	Horng & Roberts 2006.
PY5	38–63 μm magnetic separate from river sediment, Taiwan	Monoclinic pyrrhotite, quartz, goethite, lepidocrocite, chlorite	Horng & Roberts 2006.
PY6-PY9	Monoclinic pyrrhotite bearing phyllites from Taiwan metamorphic Central Range	Monoclinic pyrrhotite	Horng <i>et al.</i> 2012,
GR1-GR4	Greigite bearing mudstones, Plio-Pleistocene Lower Gutingkeng Formation, SW Taiwan	Fine-grained greigite	Horng <i>et al.</i> 1998; Jiang <i>et al.</i> 2001.
LUA-LUD	<38 μm magnetic extract from Late Triassic Lunde Fm, N. Sea.	Mn and Cr-bearing magnetites, chromite, (magnetite) oxide inclusions in various silicates.	Hounslow <i>et al.</i> 1995; Hounslow 1996
LUD2, LUD3	38–63 μm and 63–250 μm magnetic extract from Late Triassic Lunde Fm, N. Sea	Dominated by Fe-oxide (magnetite) inclusions in silicates, lesser chromite and Mn-magnetite.	Hounslow <i>et al.</i> 1995; Hounslow 1996.
OR1, OR2	<38 μm Magnetic extract from 0.35 m, 1.25 m depth in IODP 722B, Indian Ocean, Owen Ridge	Magnetite as mixed detrital and very minor bacterial magnetite. Fe-oxide inclusions in various silicates (probably minor contribution)	Hounslow & Maher 1996, 1999
OR3	<38 μm Magnetic extract from 7.8 m, depth in IODP 722B, Indian Ocean, Owen Ridge	Detrital magnetite. Fe-oxide inclusions in various silicates, ilmenite.	Hounslow & Maher, 1996, 1999
OR4, OR5, OR6	<38 μm Magnetic extract from 38.6 m, 40.6 m, 60 to 62 m in IODP 722B, Indian Ocean, Owen Ridge	Residual assemblage of detrital magnetite, ilmenite and major Fe-oxide inclusions in various silicates.	Hounslow & Maher, 1996, 1999
MR1	<38 μm Magnetic extract from 118 to 120 m in IODP Site 709A, Madingly Rise, Indian Ocean (oxic interval)	Magnetite as mixed detrital and important bacterial magnetite.	Hounslow & Maher, 1996, 1999
MR2, MR3	<38 μm Magnetic extract from 112.9 m and 28 to 29.7 m in IODP Site 709A, Madingly Rise, Indian Ocean (reduced interval)	Magnetite as mixed detrital and less important bacterial magnetite.	Hounslow & Maher, 1996, 1999
MR4	<~2 μm Magnetic extract from 5.89 to 8.41 m and IODP Site 709A, sample levels with SIRM/ χ ARM > 390 Am ⁻¹ . E_{mpt} extract.	Major bacterial magnetite with similar content of fine detrital magnetite	Maher & Hounslow 1999, unpubli. data
MR5	<~2 μm magnetic extract from 22.8 to 23.5 m in IODP site 709C, Madingly Rise, Indian Ocean. E_{mpt} extract.	Minor bacterial magnetite with larger content of fine detrital magnetite	Maher & Hounslow 1999, unpubl. data
MR6	<~2 μm magnetic extract from 45.8 to 47.3 m in IODP site 709C, Madingly Rise, Indian Ocean. E_{mpt} extract (sulphide-reduced interval)	Residual assemblage of detrital magnetite, ilmenite, and major Fe-oxide inclusions in various silicates.	Maher & Hounslow 1999; unpubl. data
CC1, CC2	Whole rock Upper Cretaceous Chalk from the level of WC9b at Culver Cliff, Isle of Wight, UK.	Rich in bacterial magnetite in chains, no detrital oxides, but common Fe-oxides as inclusions in silicates.	Montgomery <i>et al.</i> 1998; Kopp & Kirschvink 2008
SVD1, SVD2	Fine-grained dolerites from the Diasbasoddon suite of the High Arctic province, sills near lower contacts at Botneheia, Svalbard	TM (20–31)–ilmenite intergrowths, altered to maghemite at margins. 1–500 μm in size; Low alteration, SD–MD behaviour. Maybe minor pyrrhotite. $T_c = 520\text{--}550\text{ }^\circ\text{C}$	Halvorsen 1973; Vincenz <i>et al.</i> 1984; Nejbart <i>et al.</i> 2011.
DF1 to DF6	Sandstones, siltstones, De Geerdalen Fm, Svalbard. DF1, DF2 from central Spitsbergen, DF3, DF4 from Hopen, DF5, DF6 from E. Svalbard.	Detrital magnetite, $T_c \sim 450\text{--}600\text{ }^\circ\text{C}$, in part oxidized, possibly wide range of grain sizes.	Hounslow <i>et al.</i> 2007, 2022.

Synthetic samples have been much used in previous RRM studies (Edwards 1980a, b; Potter & Stephenson 1986; Snowball 1997b; Madsen 2003), but the intention here was to focus on naturally derived materials, since synthetic samples can have unusual morphologies, microstructure and purity not seen in natural minerals.

To prepare samples of the magnetic extracts and detrital pyrrhotite to measure they were dispersed in a 5 ml droplet of PVA glue on an acetate sheet, which was allowed to dry at room temperature

overnight. When dry this was peeled off, folded into a ball, and placed in a plastic pot (with cling-film padding) as the sample to measure. There was some inevitable clumping of magnetic particles during the drying process, an inevitable consequence of using granular magnetic materials, which will have resulted in some magnetic interaction (clumping observed in most) and anisotropy affects (Cisowski 1981). The pyrrhotite bearing phyllites were gently crushed and mounted in a plastic pot. Other samples were core-plugs or cubes with no encapsulation.

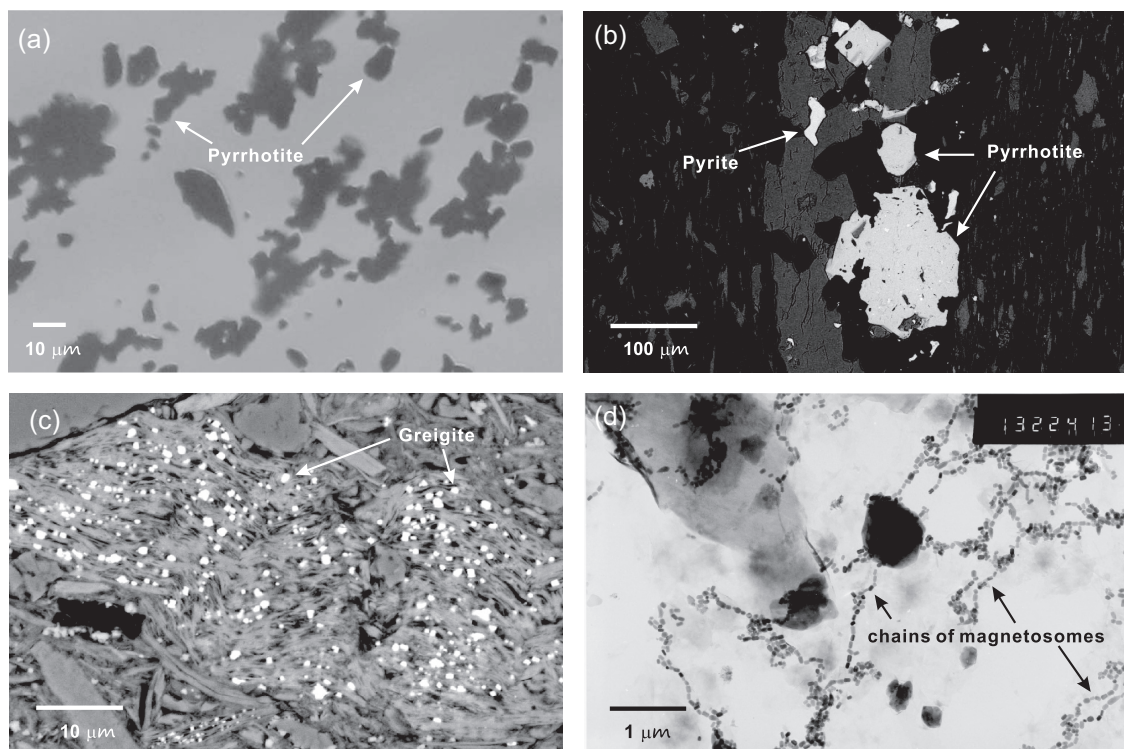


Figure 2. Example micrographs of some of the test samples. (a) Optical reflected light micrograph of sample PY2 (5–10 μm detrital monoclinic pyrrhotite magnetically separated from river sediment). (b) Backscatter scanning electron microscope (BSE) image of pyrrhotite bearing phyllite. The brightest phase is pyrite, and the more abundant slightly greyer phase is pyrrhotite, both embedded in a fine-grained phyllosilicate-quartz matrix. (c) BSE image of *ca.* $0.5 \mu\text{m}$ in size, brighter greigite embedded in a clastic-phyllosilicate rich matrix. (d) Transmission electron microscope image of chains of magnetofossils in a magnetic extract from Chalk sample at level of CC2. See the Supporting Information for more details on the test samples.

4 EXPERIMENTAL PROCEDURES AND ISSUES

Measurements used the Lancaster University RAPID magnetometer. This RAPID is housed in a large Helmholtz cage for field cancellation, which together with the Mu-metal shields cancels the earth's magnetic field to around 0.03–0.08 μT at the demagnetizer coil position. AF frequencies are 327 Hz on the transverse-axis coil (Fig. 1), and 360 Hz on the Z-axis coil. The Lancaster RAPID has a standard duration of peak AF field of 30 AF cycles giving hold times (T_H) of 92 and 83 ms for transverse and Z-axis coils, respectively. T_H can be changed but is kept low to limit coil overheating. The ramp-up and ramp-down times are fixed at *ca.* 0.64 s and 1.53 s (i.e. T_D), respectively, irrespective of maximum field used (See Supporting Information Section 4 for further details).

The RAPID vacuum system that holds samples onto the silica glass rod for insertion into the measurement space, is unable to routinely hold-onto rock samples at $\omega > 3 \text{ Hz}$ [rps], unless special precautions are taken to fix the sample onto the quartz-glass rod. This essentially limits the routine practical RRM measurements of usual-sized rock samples to rotation rates of $\leq 3 \text{ Hz}$ [rps]. The software set 'rotation rate' is half that actually achieved (i.e. set values of 1, 2, 6 correspond to 0.5, 1 and 3 Hz [rps], respectively). This was calibrated at rotation rates 0.1, 0.15, 0.2 Hz [rps], which yielded a linear relationship with time, and extrapolated to rates up to 3 Hz [rps].

All weak magnetization measurements were performed with a 'measurement blank' appropriate for each sample set (i.e. a blank

subjected to all the same steps). This bypassed the 'standard holder-correction procedure' on the RAPID, which does not account for magnetization and demagnetization of holders and sample pots during measurements. The GM4Edit software does the blank-type corrections to the data (Hounslow 2019).

All samples were set into an initial standard state by AF demagnetization, sequentially along magnetometer X , Y axes at 110 mT, followed by demagnetization only along the Z-axis at 150 mT. A larger field along Z-axis was applied to reduce possible GRM's along the Z-axis from the X and Y AF applications, which can persist into higher coercivity fields than the applied field (Edwards 1982b; Madsen 2003). All RRM and ARM_{ROT} measurements were performed with a 100 mT peak AF field. Here the sign of ω indicates the sense of spin coded into the RAPID software. A $-\omega$ rotation rate has the rotation vector directed **down** (to $+Z$), and $+\omega$ rate the rotation vector directed **up** (to $-Z$; Fig. 1). The sign of ω therefore also indicates the down or up-sense of the rotation vector. Hence, positive RRM will be a larger magnetization along the Z-axis with a $-\omega$ rotation rate (vice versa for a negative RRM; Fig. 1). It is implicitly assumed that at 1 Hz [rps] one rotation corresponds to 327 cycles of the transverse AF field.

RRM generation follows the procedure of Wilson & Lomax (1972) in which the sample was sequentially spun in opposite senses (first about the Z-axis with $-\omega$). The RRM is $\frac{1}{2}$ the difference between the magnetization measurements at $+\omega$ and $-\omega$ (Fig. 1). The sample spins throughout the AF ramp-up, hold and ramp-down interval. Other AF fields use the same hold and ramp-down times, but the AF ramp-down-rate (i.e. mT s^{-1}) is adjusted to fit these times

(inset in Fig. 1). For weak RRM's it is often advantageous to perform repeats, since the noise inherent in determining the RRM can be larger than the magnetization measurement standard deviation (SD) along the Z-axis (see Supporting Information for noise details). This problem is amplified if there is residual undemagnetized remanence (e.g. from >150 mT coercivity remanence) along the Z-axis, since the SD of magnetization measurements along any axis is strongly related to the moment along that axis (Fig. S10). In a practical sense this dictates: (1) the lower limit of useful RRM measurement for those samples with a significant intrinsic remanence which cannot be AF demagnetized. That is, the presence of significant haematite or goethite-magnetizations limits the applicability of using RRM (as does very low abundances of magnetic minerals). (2) The RRM and ARM_{ROT} measurements should be performed prior to any other large field magnetizations.

The ARM_{ROT} is determined with a DC bias field of 100 μ T along the Z-axis (AF of 100 mT along the Y-axis; Fig. 1), and by spins in opposite senses (spun about Z-axis with $-\omega$ first; Fig. 1). The ARM_{ROT} is the average of the two magnetization measurements. Theoretically, the difference between these two should also yield the RRM (Stephenson & Molyneux 1987, here symbolized as RRM_{100}), although in practice the additional large ARM_{ROT} makes the determination of RRM_{100} noisier than without the DC field (Supporting Information Section 3.2). In addition, we used the same field settings and measured the ARM acquired at zero rotation rate (ARM_{TRAN}). This could be used as a proxy for ARM_{ROT} , if equipment was not available to rotate samples during ARM acquisition (this is examined in Supporting Information Section 3.1). Rotational ARM can also be produced by rotating samples in orthogonal weak and strong and declining DC fields as an alternative (Stephenson 1988). A conventional ARM was also determined along the Z-axis by applying a 100 mT AF and 100 μ T DC coaxial along the Z-axis (called here ARM_z) allowing comparison to other standard ARM data sets. Measuring both ARM_{ROT} and ARM_z provides additional mineral-diagnostic values. Care was taken in determining the zero-level for all ARM measurements by measuring residual magnetization after AF demagnetization at 150 mT (along Z, ramp down time of 1.39 s) before and after the ARM determinations (see Supporting Information for details).

For the magnetic extracts a blank comprising a dry PVA droplet + pot + quartz-silica rod has a mean RRM of $\sim -0.10 \pm 0.2 \times 10^{-10}$ Am² (at 0.5 Hz [rps]), ARM_{ROT} of $\sim 1.7 \pm 0.5 \times 10^{-10}$ Am² (at 0.5 Hz [rps]), and 150 mT demagnetized Z-axis moment of $\sim 0.4 \pm 0.3 \times 10^{-10}$ Am² (uncertainties are 1σ). The RAPID quartz-silica rod used has a mean Z-moment of $\sim 0.15 \pm 0.4 \times 10^{-10}$ Am² (1σ , after 150 mT demagnetization). The average uncertainty (1σ) of a single magnetization measurement (average of four in total on the Z-axis) for the quartz-silica rod is $\sim 0.01 \times 10^{-10}$ Am².

The median destructive field (MDF) of the RRM was determined in two ways: (1) after RRM acquisition from the $+\omega$ rotation state (followed by static AF demagnetization along the Z-axis in 10 mT increments, up to 90 mT, followed by one at 150 mT) and (2) for both $+\omega$ and then $-\omega$ rotation states (both with static AF demagnetization on Z-axis, in 10 mT increments to 150 mT).

In method-1 the zero-'base line' of the RRM decay was judged using the flat-tail of the RRM decay curve and the 150 mT step. In method-2, by subtracting the $+\omega$ and $-\omega$ RRM demagnetization curves, and estimating the zero-'base line'tail of the resulting RRM decay (see Supporting Information for details). In each case a linear regression trend using a few data points either side of the MDF was fit to the normalized moment to field intensity changes, from

which the median point was estimated in Excel. The MDF of the ARM_z was similarly determined but using the two points straddling the median point. An alternative simpler proxy for the ARM stability is the proportion of ARM remaining after 40 mT demagnetization (Peters & Thompson 1998), which is here symbolized as $d.ARM_{z40mT}$. Comparison of MDF and $d.ARM_{z40mT}$ between different methods of demagnetization can be problematic, since MDF's produced by static, single axis methods can be some 1.3–1.5 times those produced by tumbling demagnetization (Stephenson 1983). For example, the seminal work of Dunlop (1983) on basalts seems to have used single axis demagnetization (West & Dunlop 1971) and that of Potter & Stephenson (1986) used tumbling. The RAPID protocol rmg-template files which run these procedures are in the Supplementary Information.

5 RESULTS

Since RRM and ARM_{ROT} vary greatly in magnitude the RRM and ARM_{ROT} are normalized by the absolute value at 0.5 Hz [rps]. This allows an intersample comparison of changes with rotation rates, removing the effect of differences in magnetic mineral abundance. The reasons for using this somewhat arbitrary value for normalization are outlined in Section 5.3.

5.1 Changes of RRM, ARM_{ROT} and Bg with rotation rate for magnetite

Like Edwards (1980b) we find the RRM has predominantly negative values throughout the rotation rate range (Figs 3a, 4a and 5a). This is except for sample SVD2 at $\omega > 1.3$ Hz [rps] which has a positive RRM (Fig. 4a). The 3 Hz [rps] step for CC2 (Fig. 4a) is probably subject to a small flux jump on the RAPID, hence its erroneously large, normalized value. One of Edwards' (1980b) samples F37B-1a shows a similar behaviour to SVD2, although a sister specimen measured by Wilson & Lomax (1972)—F37B-2 did not. Most of the samples display a minimum in RRM between 0.3 and 0.4 Hz [rps]. Minimums have typically also been found in other magnetite bearing rocks at low, but differing rotation rates (Potter & Stephenson 1986; Stephenson & Snowball 2001). This general pattern is consistent except for sample MR2 (rather noisier data), which has a rather flatter RRM- ω curve (Fig. 3a), like specimens E23a-1 and L-S1-2 of Wilson & Lomax (1972).

The normalized ARM_{ROT} have mostly rather flattish curves with a small decline in ARM_{ROT} at $\omega > 0.3$ Hz [rps] for the magnetic extracts and the dolerite samples (Figs 3b and 4b). Contrastingly rather steeply declining ARM_{ROT} for larger ω occur for the Chalk and De Geerdalen sandstone/siltstone samples (Figs 4b and 5b). Significantly, ARM_{ROT} changes with ω have not been investigated much previously, although changes observed have been inferred as an interaction between the RRM and the ARM_{ROT} (Stephenson & Snowball 2001). The transverse ARM produced without rotation (ARM_{TRAN}) is most often slightly lower than that produced at $\omega = 0.05$ Hz [rps] (Figs 3b, 4b and 5b).

Normalized Bg values largely mirror the changes in normalized RRM for many samples especially those with a negative peak in Bg less than -3μ T (Figs 3c, 4c and 5c). The two Chalk samples (CC1, CC2) show the flattest curves and lowest Bg values between 0 and -1μ T throughout the rotation rate range (Fig. 4c). The changes in Bg with ω are rather noisy due to weak RRM's for MR2 and OR3 (Fig. 3c) and are perhaps closer to Bg behaviours shown by SVD1, DF2, DF5, DF6 which have stronger RRM's (Figs 4c and 5c).

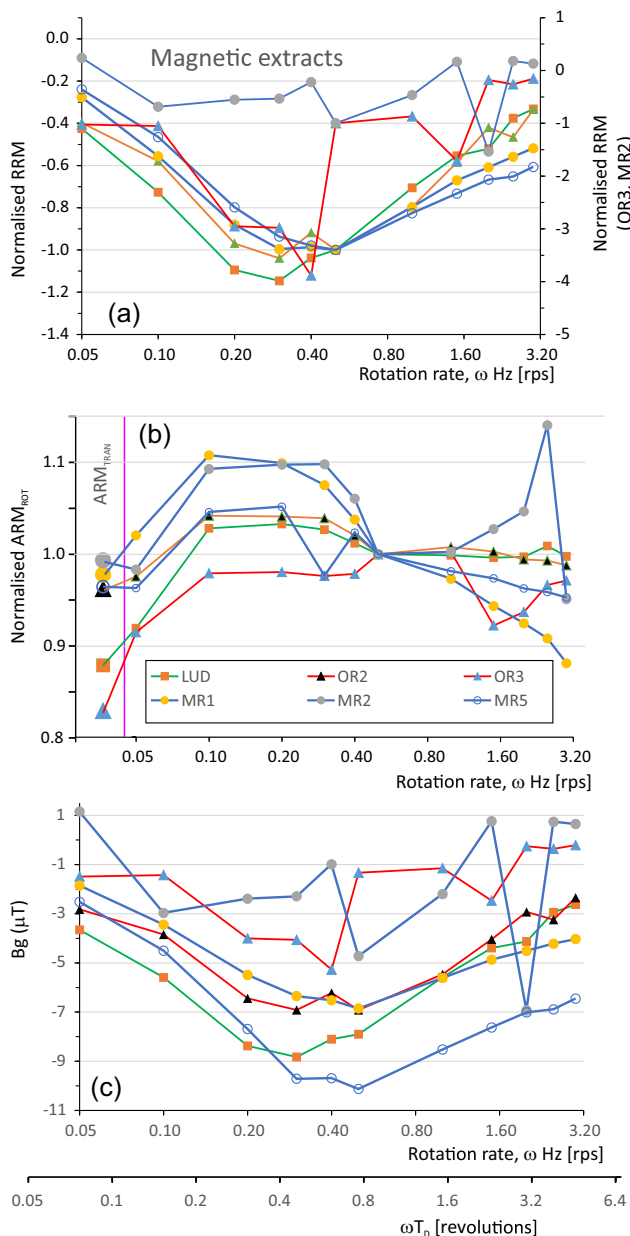


Figure 3. Magnetic extract samples LUD, OR2, OR3, MR1, MR2 and MR5. Variation of: (a) normalized RRM, (b) normalized rotational ARM (ARM_{ROT}) and (c) B_g with revolution rate (ω in Hz [rps]). In (a) and (b) the absolute value for that at 0.5 Hz [rps] is used for normalization. In (a) sample OR3, MR2 share the right-hand scale. The legend in (b) applies to all subpanels. In (b) is the ARM generated in the same way as the RRM, but with zero rotation (ARM_{TRAN}). Additional scale in (c) is ωT_D (in revolutions), where T_D is the decay time of the AF field in seconds.

The lower B_g values for the magnetite magnetofossils in the Chalk samples compared to the silt-sized magnetic extracts are opposite to the negative relationship with magnetic grain size noted by Potter & Stephenson (1986) for crushed and sized-magnetite. Chen (2014) also noted the *ca.* 10–100 times smaller B_g values for several sets of magnetite magnetosome samples compared to the samples measured by others at high spin rates (Table 2). The measurements here therefore concur with those of Chen (2014), although ability to directly compare B_g values between low and

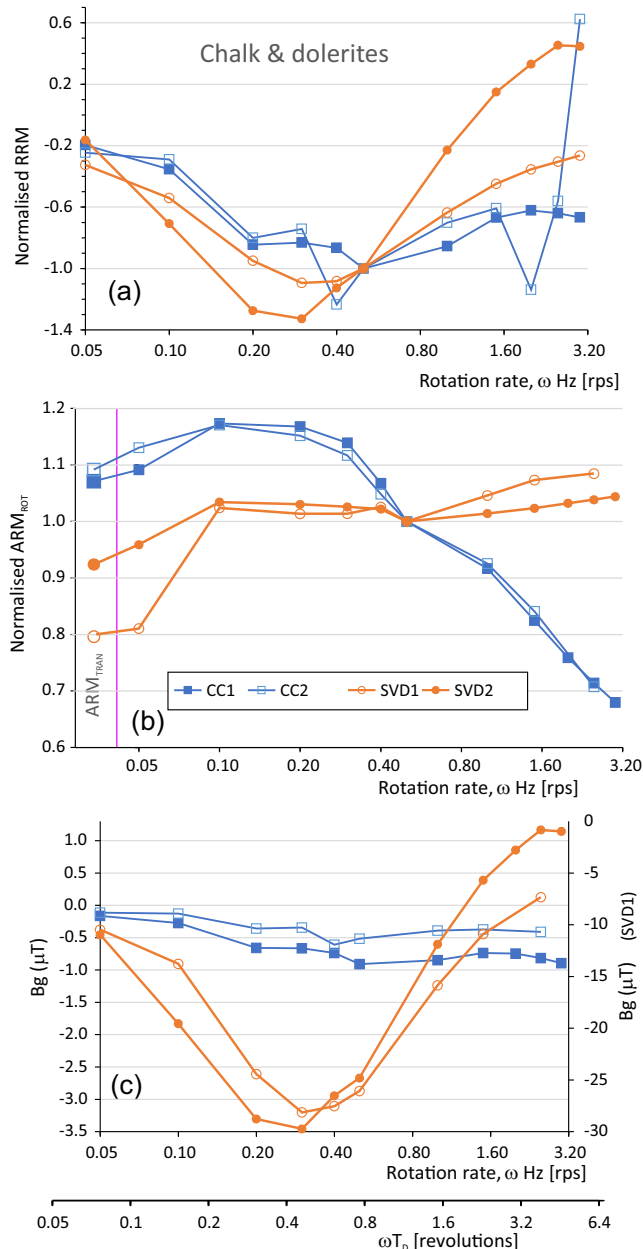


Figure 4. Chalk (CC1, CC2) and dolerite (SVD1, SVD2) test samples. In (c) only sample SVD1 has a separate scale for B_g . See Fig. 3 caption for details.

high spin data sets is hindered. The sample Pajep8 of Snowball (1997b) containing magnetite magnetofossils and MD magnetite with a B_g of $-0.14 \mu T$ at 5 Hz [rps] (Table 3) is also consistent with these observations.

The B_g values and changes with ω for samples from the De Geerdalen Formation are rather like the magnetic extracts (Figs 3c and 5c), a feature which might be expected considering initial sulphidic diagenesis typically removes much of the finer grained discrete magnetite content in sediments (Roberts 2015). Compared to the other samples, dolerite SVD1 has a much larger B_g value ($-26 \mu T$ at 0.5 Hz [rps]). Edwards & Desta (1989) have measured similar values in synthetic γFe_2O_3 ($-30 \mu T$, $-37 \mu T$; Table 3) and Roperch & Taylor (1986) in a Miocene basalt sample ($-25 \mu T$) at low ω .

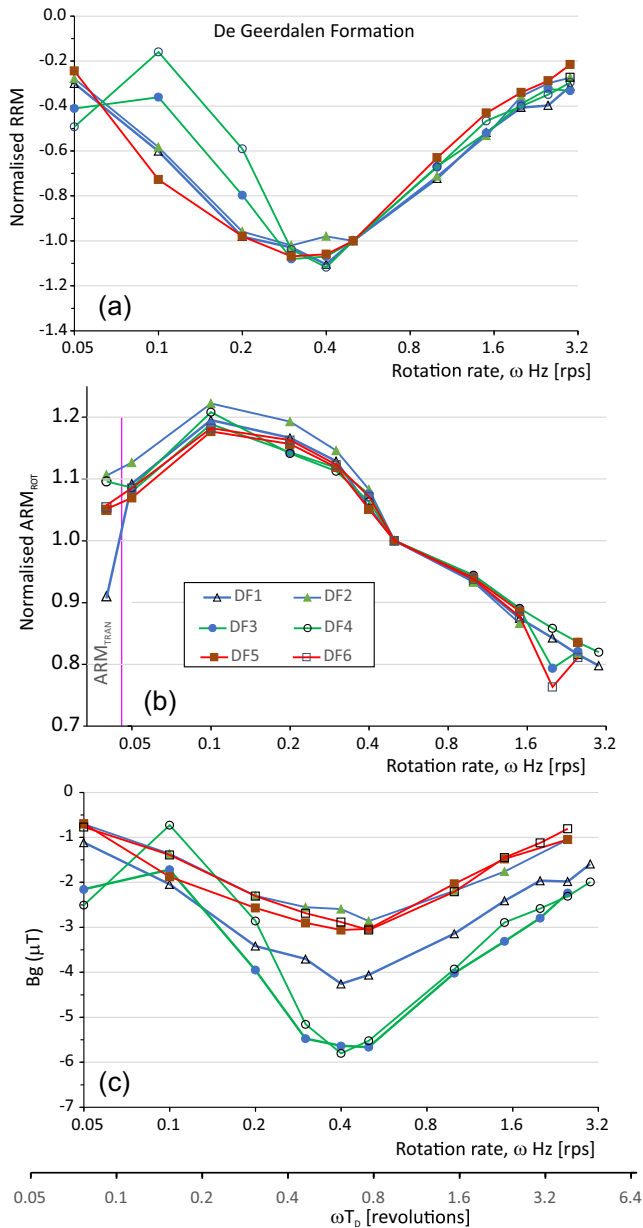


Figure 5. De Geerdalen Formation test samples DF1 to DF6. See Fig. 3 caption for details.

5.2 Changes of RRM, ARM_{ROT} and B_g with rotation rate for pyrrhotite and greigite

Greigite produces normalized RRM changes with ω like that of magnetite, but with a minimum (negative) RRM at 0.5 Hz [rps], and some larger fluctuations at lower ω values (Fig. 6a). Pyrrhotite samples do not display RRM behaviour like magnetite and greigite, having positive RRM for part or all the range of ω investigated (Figs 7a and 8a). Generally, all the pyrrhotite samples had RRM which was challenging to measure (i.e. producing noisy data), since they contained a strong residual remanence remaining after 150 mT demagnetization, so much of the sample data is from averaging of duplicate measurements. The detrital pyrrhotite $>20 \mu\text{m}$ in size (PY4, PY5) produces a peak in positive RRM at 0.3–0.4 Hz [rps], and then declines towards near zero or negative RRM by

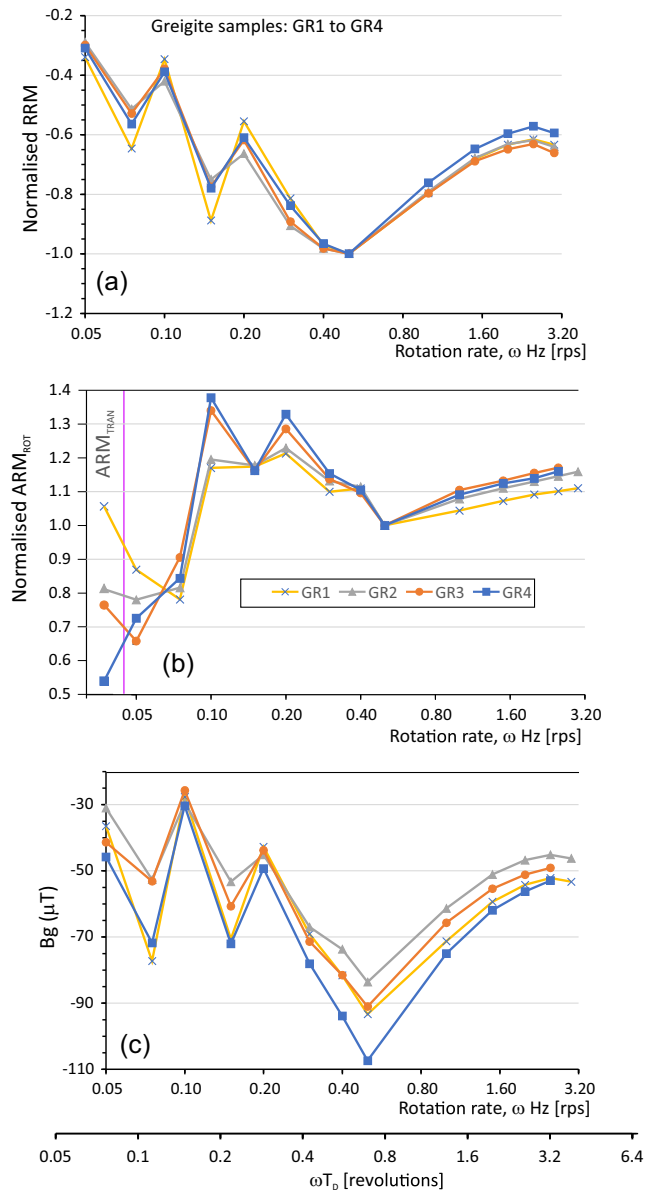


Figure 6. Greigite-bearing siltstone test samples GR1 to GR4. See Fig. 3 caption for details.

3 Hz [rps] (Fig. 7a). Detrital pyrrhotite $<20 \mu\text{m}$ (PY1–PY3) produces a trend towards increasingly more positive RRM through 0.5–2.5 Hz [rps]. The $<2 \mu\text{m}$ detrital pyrrhotite has the largest positive normalized RRM at $\omega > 1 \text{ Hz [rps]}$ and has some possible step-like behaviour in RRM at $\omega < 0.4 \text{ Hz [rps]}$, like greigite (Figs 6a and 7a)—although this may be measurement noise in this quite weak sample. The pyrrhotite-bearing phyllite samples (PY6 to PY9) show RRM behaviour with ω rather like the coarser detrital pyrrhotite (Fig. 8a) suggesting these largely contain pyrrhotite $>20 \mu\text{m}$ in size. Such large particle sizes are also seen in electron microscopy (Fig. 2b). A positive RRM was detected by Thomson (1990) in samples heated to 228–315 °C but generally much smaller negative RRM's in unheated or those heated to below 228 °C (at 3 Hz [rps]). Thomson (1990) attributed these temperature-related changes to creation of hexagonal pyrrhotite during the heating. The RRM produced by Thomson

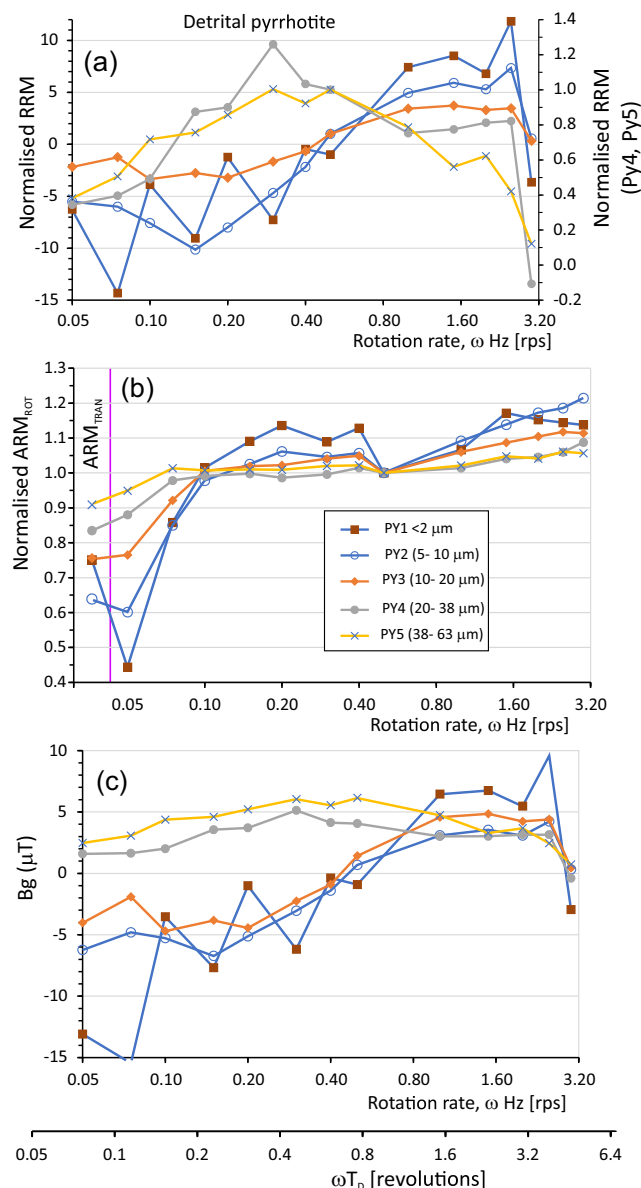


Figure 7. Sized detrital pyrrhotite test samples PY1 to PY5. In (a) PY4 and PY5 share the right-hand scale. See Fig. 3 caption for details.

(1990) was weakly if at all dependent on rotation rates at $\omega < 10$ Hz [rps].

Changes in ARM_{ROT} with ω for the sulphides are rather similar and flattish at >0.4 Hz [rps] with all showing a progressive increase in normalized ARM_{ROT} at $\omega > 0.5$ Hz [rps] (Figs 6b, 7b and 8b), and like magnetite have ARM_{TRAN} values rather similar or lower than the value at 0.05 Hz [rps].

Changes in B_g largely reflect the changes in normalized RRM, since any changes in ARM_{ROT} are rather suppressed compared to RRM changes with ω (Fig. 7C). The pyrrhotite samples show mostly positive B_g at $\omega \geq 0.5$ Hz [rps]. Slotznick *et al.* (2016) has apparently detected a range of both positive and negative B_g values in pyrrhotite bearing rocks (at $\omega \geq 1$ Hz [rps]), although the methodology used is unclear, since their ' B_{eff} ' values seem to exist for both $-\omega$ and $+\omega$.

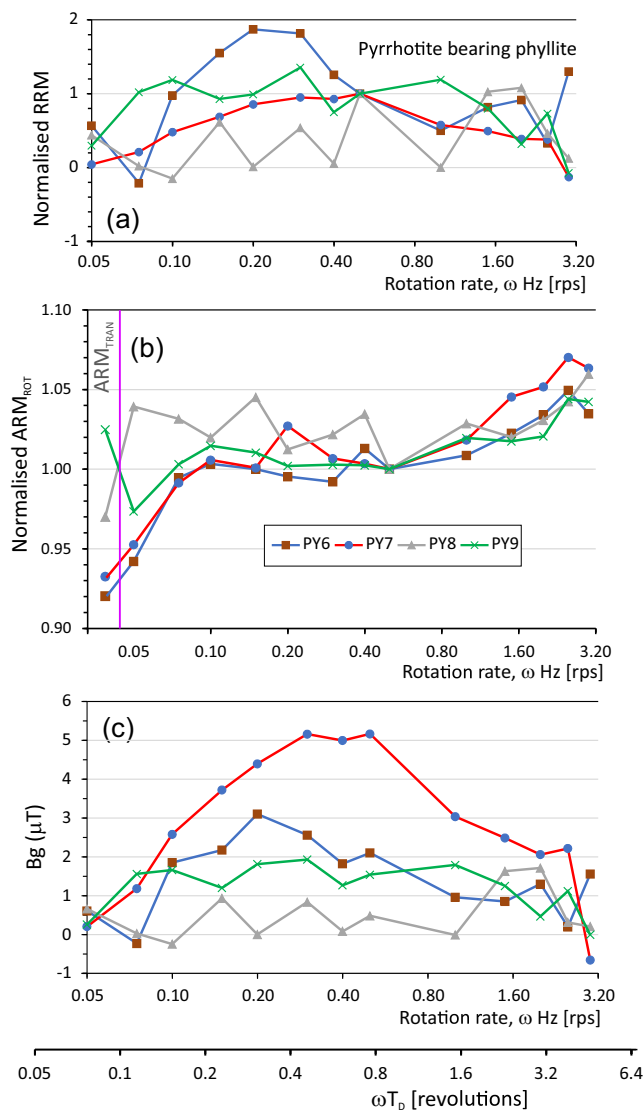


Figure 8. Pyrrhotite bearing phyllite test samples PY6–PY9. See Fig. 3 caption for details.

5.3 Impact of changing AF field hold times on RRM and ARM_{ROT}

Edwards (1982b) demonstrated that for magnetite the AF field ramp down time (T_D , in seconds) controlled the position of the peak of the negative RRM in magnetite-bearing samples, such that ωT_D (in revolutions, or rev for short) was a more fundamental expression of the RRM changes than the rotation rate. For the magnetite-bearing samples of Edwards (1982b) the peak in negative RRM was at 0.40 ± 0.02 rev. The apparent peak in our magnetite-bearing samples is at $\omega T_D = 0.4$ to 0.75 rev (Figs 3–5), generally somewhat larger than Edwards observed. However, our RRM initialization is different to that used by Edwards, since our hold time, T_H (92 ms) is insufficient to produce the 90° of rotation initialization used by Edwards. For three samples we measured RRM and ARM_{ROT} with rotation rate for T_H at 0.917 and 9.17 s (300 and 3000 cycles setting on RAPID; Fig. 9). A T_H of 0.917 s produces the required 90° (or larger) of initialization rotation at $\omega \geq 0.27$ Hz [rps], ($\omega T_D = 0.42$ revolutions or larger using $T_D = 1.53$ s) and a T_H of 9.17 s exceeds the 90° threshold at all rotation rates used (Figs 9a, c and e). Both these larger T_H produce a peak in RRM close to $\omega T_D = 0.4$ rev

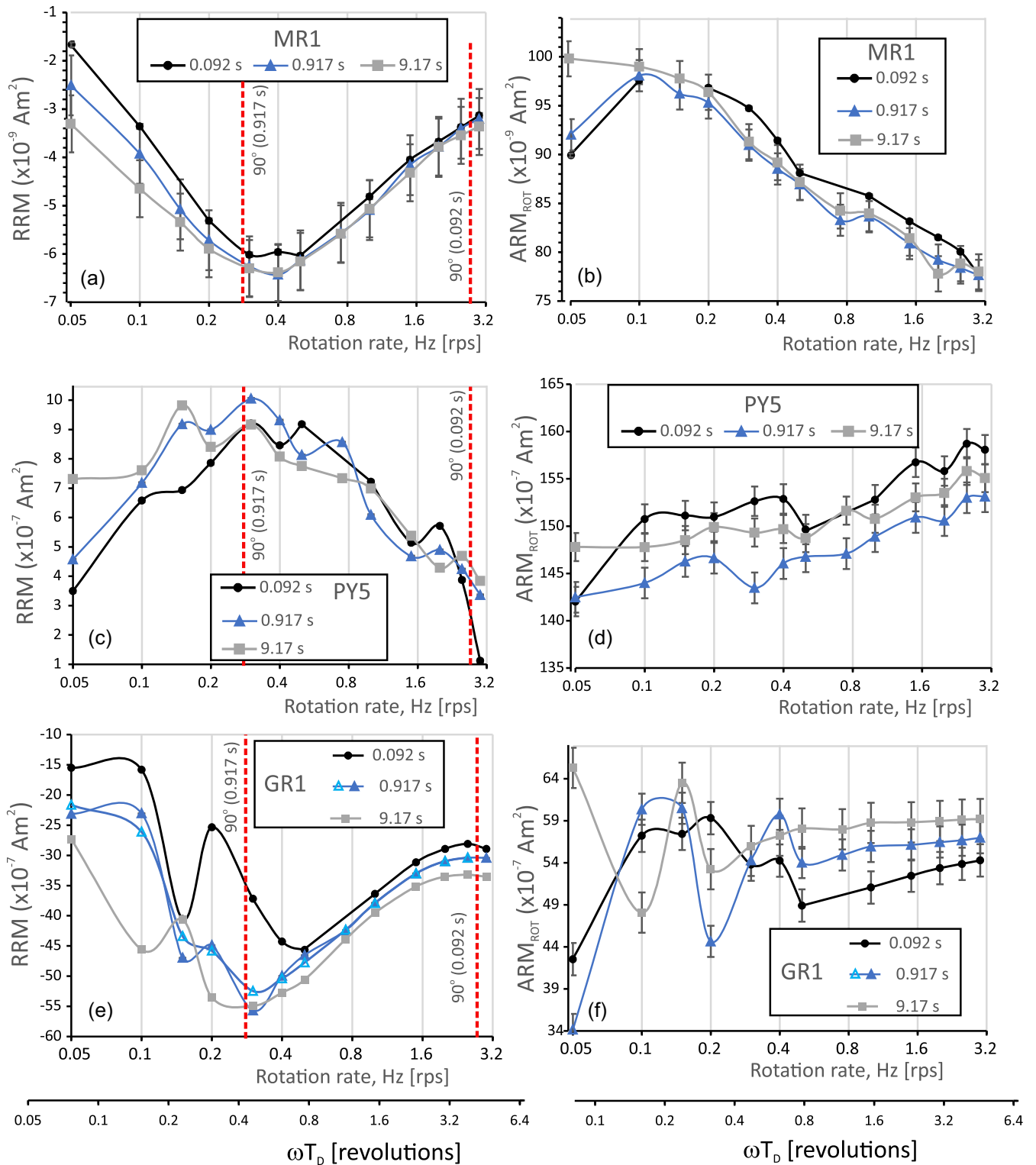


Figure 9. RRM and ARM_{ROT} of test samples with three AF field hold times (T_H) of 0.092, 0.917 and 9.17 s. Panels (a, b) are for magnetite sample MR1; panels (c, d) for pyrrhotite sample PY5 and panels (e, f) for diagenetic greigite sample GR1. The dotted vertical red lines in (a, c, e) are the rotation rate thresholds at which the two smaller T_H values have full 90° of rotation at the maximum field of 100 mT. The longest hold time of 9.17s achieves 90° rotation at maximum field even at 0.05 Hz [rps]. Error bars are the 1σ uncertainty (smaller than symbols in c and e) from the remanence measurement. Most of the uncertainty in (b), (d), (f) relate to the uncertainty in the zero level of the ARM_{ROT}. Points are connected by an Excel fitted ‘smoothed-curve’.

for pyrrhotite and greigite (Figs 9c and e), as does dolerite sample SVD2 (Fig. S19b), but the magnetite sample MR1 has its RRM peak at 0.6 rev (0.4 Hz [rps]; Fig. 9a). These data broadly concur with Edwards (1982a) experimental data but do suggest that perhaps there may be additional mineralogical control on the precise position of the RRM peak in ωT_D units.

Broadly the RRM using $T_H = 92$ ms are a little smaller than that acquired over longer hold times at rotation rates 0.5–3 Hz [rps], and diverge more at rates <0.5 Hz [rps] (Figs 9a, c and e). For the magnetite (MR1) and pyrrhotite (PY5) samples at $\omega = 0.3$ –3 Hz [rps], the RRM at 92 ms hold time is some 96 ± 1.6 per cent and 105 ± 13 per cent (1σ values) of that for the average of RRM at the longer hold times. Greigite (sample GR1) in contrast, has RRM some 88 ± 3 per cent of the RRM for $T_H = 9.17$ s, over the 0.5–3 Hz [rps] range (Fig. 9e), but substantial deviations at rates <0.5 Hz [rps] (Fig. 9e). The greigite RRM is more consistent between the 0.917 and 9.17 s hold times at $\omega \geq 0.3$ Hz [rps] above the 90° initialization threshold (Fig. 9e).

For magnetite (MR1) and pyrrhotite (PY5) the ARM_{ROT} (for $T_H = 92$ ms), is on average marginally larger than both the longer hold times (Figs 9b and d), with the average percentage comparison being 102 ± 1.4 per cent, 104 ± 1.2 per cent for $T_H = 0.917$ s and 102 ± 1.4 per cent, 102 ± 1.1 per cent for $T_H = 9.17$ s, respectively (for $\omega = 0.1$ –3 Hz [rps]). In contrast, greigite displays lower ARM_{ROT} at $T_H = 92$ ms with the average comparison being 93 ± 2.0 and 89 ± 2.9 per cent for the 0.917 s and 9.17 hold times (at $\omega \geq 0.5$ Hz [rps]). The greigite (GR1) behaviour at $\omega < 0.5$ Hz [rps] is quite different to the other samples and indicates a complexity in ARM_{ROT} acquisition not seen in other test samples. The impact of T_H differences on Bg are like those percentage comparisons seen in RRM for magnetite (MR1) and pyrrhotite (see Fig. S19). For greigite sample GR1, the peak in Bg is also larger at $\sim 102 \mu\text{T}$ and displaced to ~ 0.2 to 0.3 Hz [rps], compared to that in Fig. 6(c).

The complexity in the RRM and ARM_{ROT} behaviour at $\omega < 0.5$ Hz [rps] (also having the AF hold time (T_H) shorter than the optimum for RRM initialization), led us to choose a blanket normalization for parameters at 0.5 Hz [rps], like is displayed in Figs 3–8. Values at this rotation rate (and larger) generally show more consistent changes. Had we used a T_H of ~ 0.92 s a more optimum value to normalize the RRM, ARM_{ROT} and Bg values would have been that close to the peak in RRM at $\omega T_D \approx 0.4$ revolutions (i.e. about 0.26 Hz [rps]). Hence, the optimum hold time on the 327 Hz RAPID demagnetizer is a T_H of 0.962 s (314 cycles) which would detect the maximum RRM at $\omega T_D \cong 0.4$ rev (0.26 Hz [rps]) at $T_D = 1.53$ s). However, this has consequences for potential excess coil heating, and the increased refinement has only minor impact on magnetite and pyrrhotite parameters. However, this is a bigger issue for samples containing diagenetic greigite (i.e. Figs 9e and f).

We suspect the RRM behaviour at $\omega < 0.5$ Hz [rps] of greigite sample GR1 (at $T_H = 92$ ms) is due to anisotropy and its impact on RRM and ARM_{ROT} acquisition (Potter 2004) at values below the rotation initialization threshold. Although, we could not investigate the directional dependence of RRM and ARM_{ROT} on GR1, we performed a preliminary study on sample SVD2 which shows similar behaviour to GR1 when rotation was used about the other two axes of this cubic sample, to generate the RRM (see Supporting Information Section 3.4). For SVD2 this impacts the RRM and ARM_{ROT} and Bg values, demonstrating that anisotropy is an additional source of changes in Bg with ω . However the pattern of changes in Bg, ARM_{ROT} and RRM are similar with respect to ω , if above the rotation initialization threshold (Fig. S19).

In a practical sense these issues suggest the reliable range of ω for routine use on the RAPID is 0.26 and 3 Hz [rps], if using an AF hold time sufficient to reach rotation initialization. Samples with significant ferrimagnetic anisotropy will have RRM-data most-impacted if there is inadequate rotation initialization. However, for many samples with weak anisotropy the AF hold-time may have a limited impact especially at $\omega \geq 0.5$ Hz [rps].

5.4 Demagnetization of the RRM

Demagnetizing of the RRM using method 1, produces an additional ‘nuisance’ magnetization created in most samples, since the ‘background’ 150 mT demagnetization on the Z-axis and the mean of the two RRM magnetization measurements (in opposite rotation directions) were not similar. This is demonstrated well by the greigite sample GR1, measured using method 2, which shows this effect very strongly (Fig. 10a), in which coincident with the RRM demagnetization, an additional magnetization (referred to here as GRMz) is generated during demagnetization along the Z-axis. This seems to be a GRM since in the X-Y plane the GRM begins to increase around the start of the GRMz increase (Figs 10a and d). Overall, the GRMz generated are mostly negative (up-directed) magnetizations (Figs 10b–d), although sometimes are positive like the demagnetization of the 0.5 Hz [rps] RRM for sample GR1 (Fig. 10a). Co-axial demagnetization axis and GRM’s have been observed previously in greigite (Hu *et al.* 1998, 2002) and magnetite (Stephenson 1981; Roperch & Taylor 1986), and these are thought to be more generally produced using static demagnetization, due to the angular dependence (with respect to grain anisotropy) of the switching field (Madsen 2003; Finn & Coe 2020). Normalizing GRMz by ARM_{ROT} in the same way as for the RRM (eq. 1), produces the effective field BgZ in μT for this remanence (in this case $BgZ = 100 \mu\text{T} \times GRMz/ARM_{ROT}$). BgZ values are similar but rather smaller than Bg for RRM induction (Fig. 11a). This is not an ARM from the residual DC field inside the demagnetizer shield, since GRMz is both positive and negative and is variable with respect to ARMz (Fig. 11b). The DC field inside the shield should produce an ARM of less than ~ 0.1 per cent of the ARMz, which is much smaller than the observed GRMz (Fig. 11b). It is also possible that this nuisance remanence may be generated by asymmetry in the AF field, generating an ARM, since small ~ 0.03 per cent asymmetry could produce an ARM of this order or larger (Hailwood & Molyneux 1974). However, the variable magnitude with the respect to the ARMz and ARM_{ROT} and the change to opposite direction for some samples, suggests this is less likely than a coaxial GRM.

Therefore, for effective determination of RRM stability (median destructive field, MDF, etc.) of the RRM the most effective way is to demagnetize both the $+\omega$ and $-\omega$ produced RRM, up to maximum fields well beyond the AF inducing field used for the RRM. This allows separation of any coaxial magnetization produce along the demagnetization axis, such as GRM’s or spurious ARM’s produced along that axis. An added advantage is that RRM’s can be quite weak in many earth materials, and the resulting RRM demagnetization curve has both duplicate data and is double the magnitude of a single demagnetization curve, resulting in a more robust data set to work with.

This improved RRM demagnetization (i.e. method-2) was tested on a few samples, which showed a different range of MDF of RRM compared to the MDF of ARMz (Fig. 12a). This is expected since these magnetizations activate different grain populations, with the RRM probably activating those with the higher or the same stability,

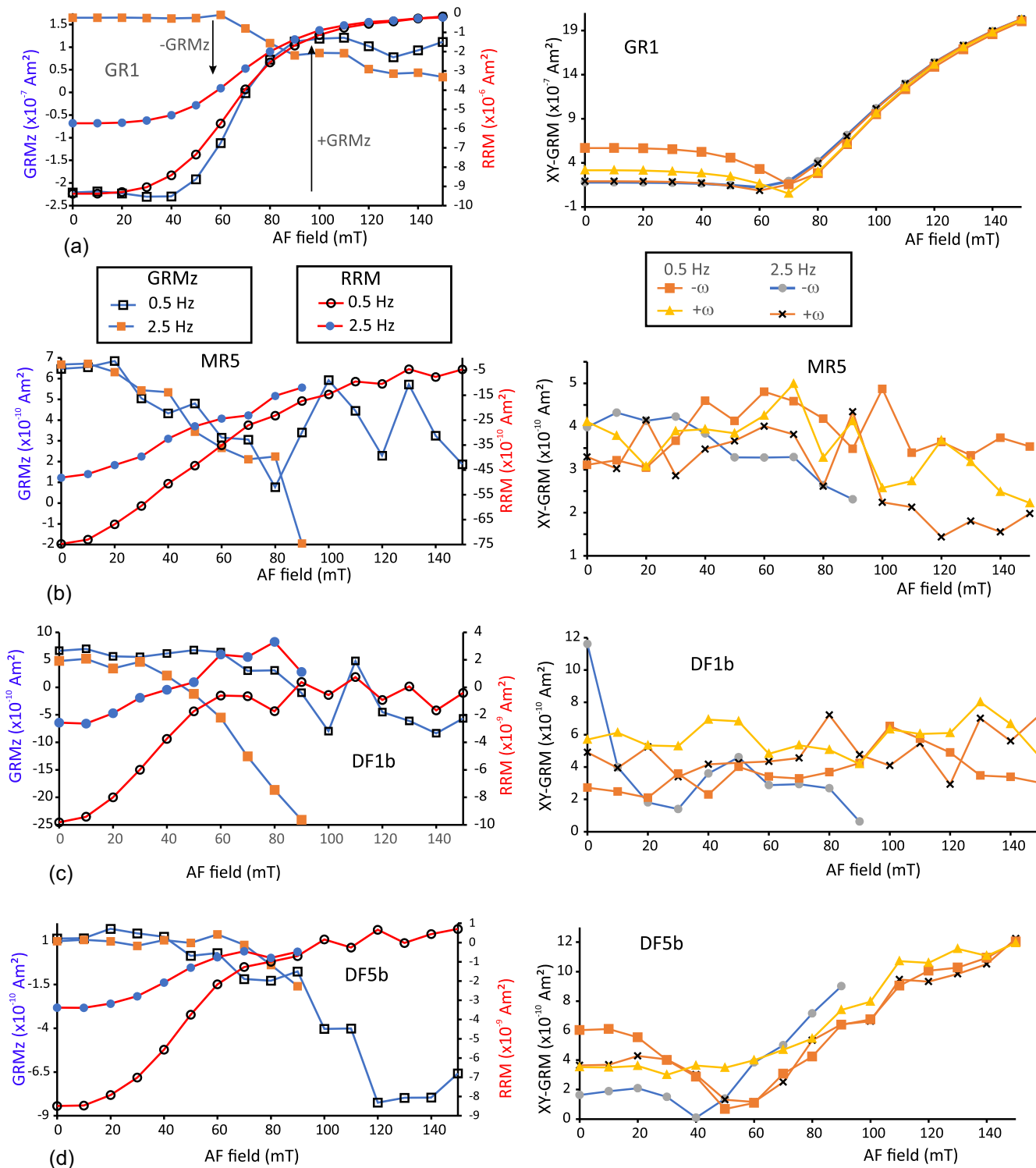


Figure 10. Example demagnetization of RRM obtained for both $+\omega$ and $-\omega$ conditions (both 0.5 Hz [rps] and 2.5 Hz [rps]). Static demagnetization is along the Z-axis parallel to the rotation axis (Fig. 1). Left-hand panels in each case show the RRM and GRMz curves in magnetic moment (Am^2) corrected for the subtraction and addition operations on the raw moments. Right-hand panels show the X-Y-axis GRM moment ($\sqrt{[X^2 + Y^2]}$) for each of the four spin measurements (two for each ω) during demagnetization. In each case the baselines have not been adjusted to zero. The measurement order is AFz demagnetization at 150 mT, RRM ($-\omega = 0.5$ Hz [rps]), progressive AF demagnetization, RRM ($+\omega = 0.5$ Hz [rps]), progressive AF demagnetization; to be followed by the same four sets at 2.5 Hz [rps]. A) Arrows show the sign of the GRMz for increasing negative, and positive values, respectively.

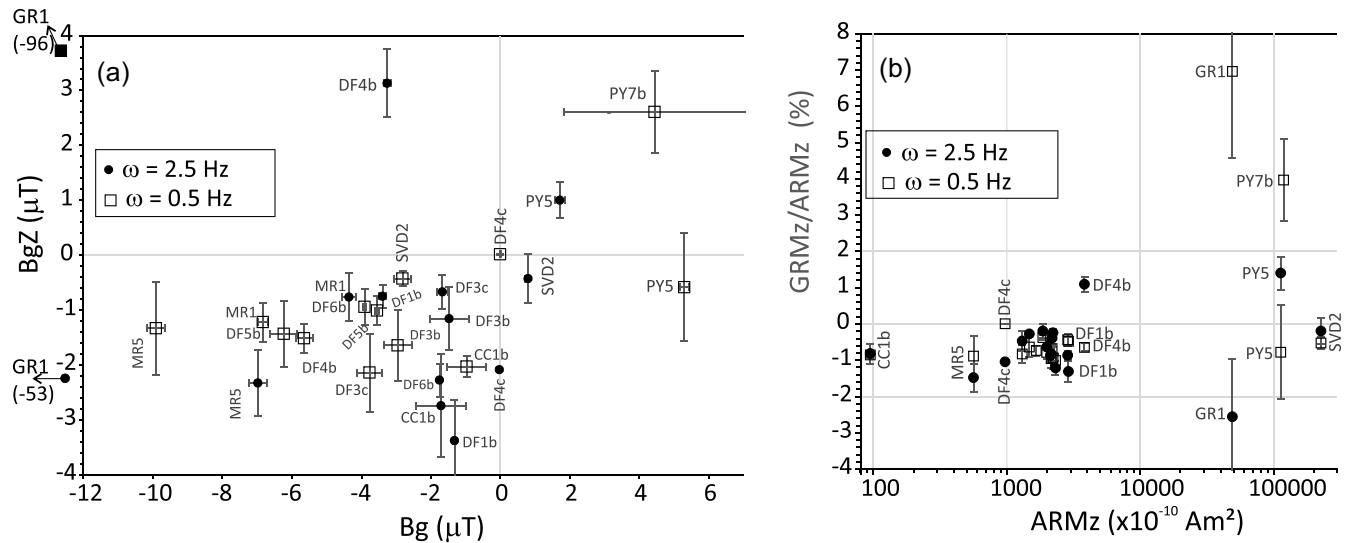


Figure 11. (a) Bg versus the effective field (BgZ) of the additional nuisance magnetization ($GRMz$) generated during static demagnetization of the RRM (i.e. Fig. 10). Data sets for both $\omega = 0.5$ Hz [rps] and 2.5 Hz [rps] are shown. Note both negative (upwards directed) and positive (downward directed) $GRMz$. Arrows indicate the off-graph positions of the greigite sample and its respective Bg values at $\omega = 0.5$ and 2.5 Hz [rps]. (b) Ratio of $GRMz$ and $ARMz$ expressed as a percentage with respect to the $ARMz$ moment. Note the often much larger % $GRMz/ARMz$ values for greigite and pyrrhotite. In each case the error bars include the RRM measurement uncertainties plus the base-line uncertainty for $GRMz$, both as $\pm 1\sigma$.

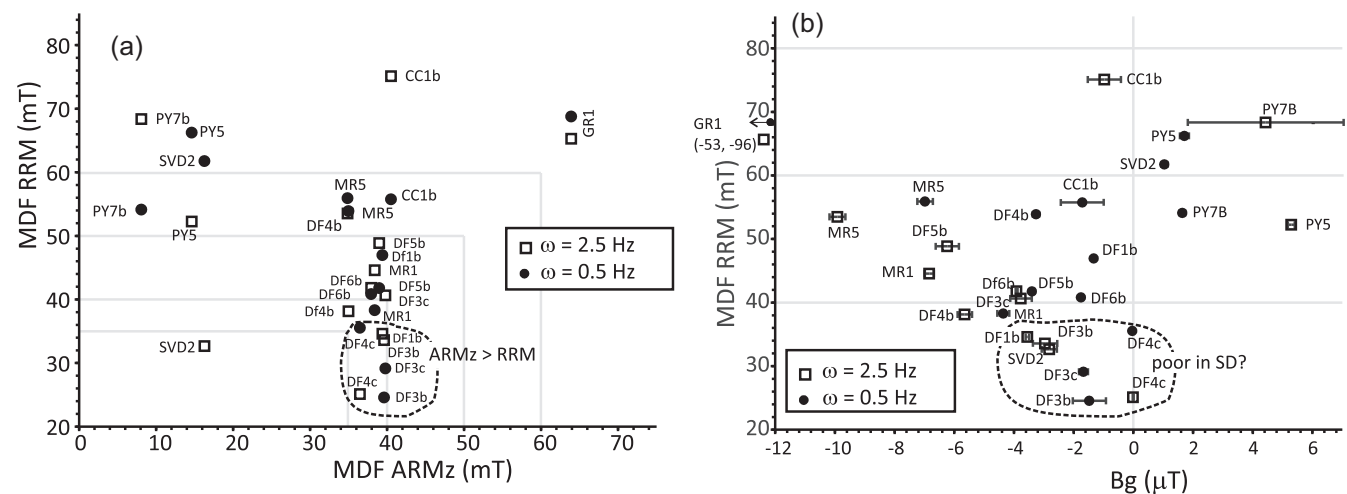


Figure 12. Median destructive field (MDF) of the RRM versus MDF of $ARMz$ in (a) and Bg in (b). This uses RRM demagnetizations using method -2 for both 0.5 Hz [rps] and 2.5 Hz [rps]. In (a) note the soft $ARMz$ (< 20 mT) of the 'large'-pyrrhotite and dolerite sample SVD2, the hard $ARMz$ (~ 64 mT) of greigite sample GR1, and the rather consistent intermediate $ARMz$ stability (35 – 41 mT) of other samples. Both the 0.5 and 2.5 Hz [rps] measurements of greigite sample GR1 plot off the X -axis in (b) at a Bg of $-53 \mu T$ and $-96 \mu T$ (Fig. 6c).

if the coercivities have a limited range to higher values (Stephenson 1976; Edwards 1984; Potter & Stephenson 1986).

There is a large range in MDF of $ARMz$ from relatively soft MD-type magnetite's with over half the remanence removed at < 15 mT (*cf.* Dunlop 1983), to many with SD-like stability with MDF of 35 – 40 mT (Dunlop 1983), to the greigite sample GR1 with the largest MDF in which half the $ARMz$ remains at 64 mT (Fig. 12a). The differing rotation rates produce rather different MDF of RRM for the same sample (Fig. 12a), with no consistent difference—approximately half (6/13) of the test samples having MDF at 0.5 Hz [rps] lower than that at 2.5 Hz [rps], and half (7 out of 13) the opposite behaviour. A subset of the De Geerdalen Fm samples (circled in Fig. 12a) have slightly lower MDF of RRM than MDF of $ARMz$,

which may in part relate to the rather larger uncertainty (order of *ca.* ± 3 mT) in estimating stability of RRM than that of $ARMz$ (< 1 mT uncertainty). Hence, the magnetite-bearing samples (except the MD-like SVD2) fall into two sets, firstly a lower stability set in which the RRM and $ARMz$ stability are similar (those with MDF of RRM $< ca.$ 42 mT; Fig. 12a) with mostly Bg from 0 to $-5 \mu T$ (circled samples in Fig. 12); and secondly a set with MDF of RRM larger than the MDF of $ARMz$ and a wide range of Bg (Fig. 12b). The two magnetite bearing samples containing common magnetofossils—CC1b and MR5 ($a < 2 \mu m$ extract), have the largest MDF of RRM for the magnetite-bearing sets (Fig. 12a), although very different Bg values (Fig. 12b). The differences between CC1b and MR5 perhaps relates to the abundant magnetofossil chains in CC1b.

The greigite sample GR1 has an MDF of RRM of 65–69 mT which is at the lowest end of the range measured for greigite by Snowball (1997b). Nevertheless, the large negative Bg in combination with the high MDF of RRM is a very distinctive feature of greigite (Fig. 12b), confirming the observations of Snowball (1997b). The large-sized pyrrhotites, PY5, PY7 (with MDF of ARMz < 15 mT; Fig. 12a) have distinctive positive Bg, and large MDF of RRM comparable to those samples with the smallest magnetite particles (e.g. MR5, CC1b; Fig. 12b).

6 DISCUSSION

6.1 Comparison with other data sets using low rotation rate

Comparison to other data sets that used low ω (less than the AF frequency) is more problematic, since AF hold and ramp-down times have been less clearly described. Potter & Stephenson (1986) used hold and decay times of 5 and 10 s, respectively, for various sized magnetite's, finding peaks in negative RRM at around 8–10 Hz [rps] ($\omega T_D \approx 80$ –100 rev), considerably larger ωT_D than seen here and in Edwards data. Peaks in negative RRM for greigite have not been recognized previously, with existing data from Stephenson & Snowball (2001) showing increasingly more negative RRM from low rotation rates until the AF-frequency threshold.

In Edwards (1982b) magnetite-based data, the negative RRM peak is followed by a trend towards more positive RRM values (both negative and positive RRM) which plateau at around $\omega T_D \approx 20$ –30 revolutions. These approximately concur with largely negative, but some positive RRM values (in basalts) measured by Roperch & Taylor (1986) for ωT_D of ≈ 30 rev (Table 3). Contrastingly, Potter & Stephenson (1986) recognized a positive peak in RRM at ≈ 20 Hz [rps] ($\omega T_D \approx 200$ rev) for crushed magnetite. Hence, it is probable that the RRM peaks and troughs seen in our data set and those of Edwards (1982b) and Wilson & Lomax (1972), between $\omega T_D = 0.4$ –30 revolutions, may be hidden in the smallest rotation rates produced by the instrument of Stephenson & Molyneux (1987) at $\omega < 3$ Hz [rps].

6.2 Mineral magnetic identification using RRM

Whilst the comparison of different Bg values at fixed Hz [rps] (or ωT_D) could be useful for simple mineral magnetic discrimination, the changes in Bg and ARM_{ROT} with ω potentially indicate a more powerful means of mineral magnetic discrimination.

There are two broad approaches that could be used for magnetic mineral discrimination using low rotation rates. The first is to use the normalized changes in RRM, ARM_{ROT} and Bg with respect to ωT_D , to build up families of curves for mineral types, granulometry and switching-field behaviours. The data in Figs 3–9 are a step in this direction. The second is to parameterize some of the key changes at $\omega T_D \geq 0.4$ rev by looking at ratios of RRM, ARM_{ROT} and Bg at say 0.5 and 2.5 Hz [rps] (ωT_D units of 0.77, 3.83 revolutions), as expression of the changes with ω . We here explore this later approach, since it potentially expresses the between-sample variability better, allowing exploration of larger data sets, and so is more easily used in palaeomagnetic studies focused on other aims.

Our somewhat limited data on RRM stability (i.e. MDF) also suggests that this may differ between rotation rates (compare test samples at 0.5 Hz [rps] and 2.5 Hz [rps] in Fig. 12). Although MDF of RRM is time consuming to measure, this may perhaps hold

some additional information for magnetic mineral discrimination in magnetically stronger samples (e.g. Fig. 12). Although not explored here, the stability of RRM is more usefully utilized in RRM build-up with increasing AF field (see SI Figs S15–S17, and Potter & Stephenson 1986; Fig. 7)—rather than demagnetization. Median acquisition is free from issues with co-axial GRM's. Alternatively, single step acquisition (say at 40 mT), as a proxy for stability, is also easy to implement and easy to use on samples displaying weak RRM that may need duplicate RRM measurements to improve accuracy.

6.2.1 Magnetic sulphides

Pyrrhotite is recognized by positive Bg at 0.5 or 2.5 Hz [rps] (Figs 7c, 8c and 13a). The Bg ratios at the rotation rates of 2.5 Hz [rps] divided by 0.3 Hz [rps] (ratios at differing ω hereafter symbolized like $\omega\{2.5/0.3\}$) can also usefully distinguish large pyrrhotite from pyrrhotite <20 μm in size (Fig. 13a); an expression of the flat-tish shapes of the RRM- ω curves (Figs 7c and 8c). An alternative parametrization is to use the ARM_{ROT} at 2.5 Hz [rps] normalized by ARMz, which clearly separates the > 1.3 values for pyrrhotite from magnetite and greigite behaviours (Figs 14a and b). Pyrrhotite is particularly challenging to identify using conventional coercivity behaviour, since it strongly overlaps the coercivity range of magnetite, and the useful normalization by magnetic susceptibility (Peters & Thompson 1998) is hampered in many sediments by paramagnetic contributions to susceptibility.

Single domain diagenetic greigite has the most distinctive signature in RRM behaviour with large negative Bg, high MDF of RRM and ARMz (Figs 12a, 14b and d). These are features also indicated by Snowball (1997b) and Peters & Thompson (1998) using ARMz. The unusually large Bg and RRM stability probably stem from the magnetic nanoscale composites that make up natural diagenetic greigite crystals (Lesniak *et al.* 2021). The change of ARM_{ROT} with ω may also be a useful feature, like also seen in the <20 μm pyrrhotite, both of which increase through $\omega = 0.5$ to 3 Hz [rps] (Figs 6b and 7b). The ratio of ARM_{ROT} at $\omega\{2.5/0.5\}$ may also be a useful and simple discriminator (Figs 13b–d and 14d).

In contrast, biogenic greigite present in magnetosomes measured by Chen (2014), appears to have low Bg values (at 95 Hz [rps]; Table 2) not much larger than for magnetite magnetosomes. However, Reinholdsson *et al.* (2013) implicated positive Bg values of 0–1 μT for greigite magnetofossils at 5 Hz [rps]. A means of using RRM to distinguish these two largely non-interacting SD grain types require more work. Perhaps the change of ARM_{ROT} with ω may be a useful signature, since magnetofossils from the Chalk show particularly dramatic declines in ARM_{ROT} with increasing ω (Fig. 4b), something that is not seen in our greigite or pyrrhotite samples. Ratios of ARM_{ROT} at $\omega\{2.5/0.5\}$ clearly discriminate the Chalk magnetite magnetofossils from other magnetite samples (Figs 13c, d and 14d). It remains to be seen if similar behaviour is also shown by greigite magnetofossils.

6.2.2 Magnetite bearing samples

It is interesting that the SD-sized magnetite in the Chalk sample set has consistently the smallest negative Bg values, opposite to the behaviour indicated by the crushed magnetite sample set used by Potter & Stephenson (1986). The small Bg values for the magnetofossils in the Chalk-samples are consistent with the work on magnetite magnetosomes by Chen (2014) at high spin rates. An explanation for the low RRM acquisition in intact magnetofossils/magnetosomes

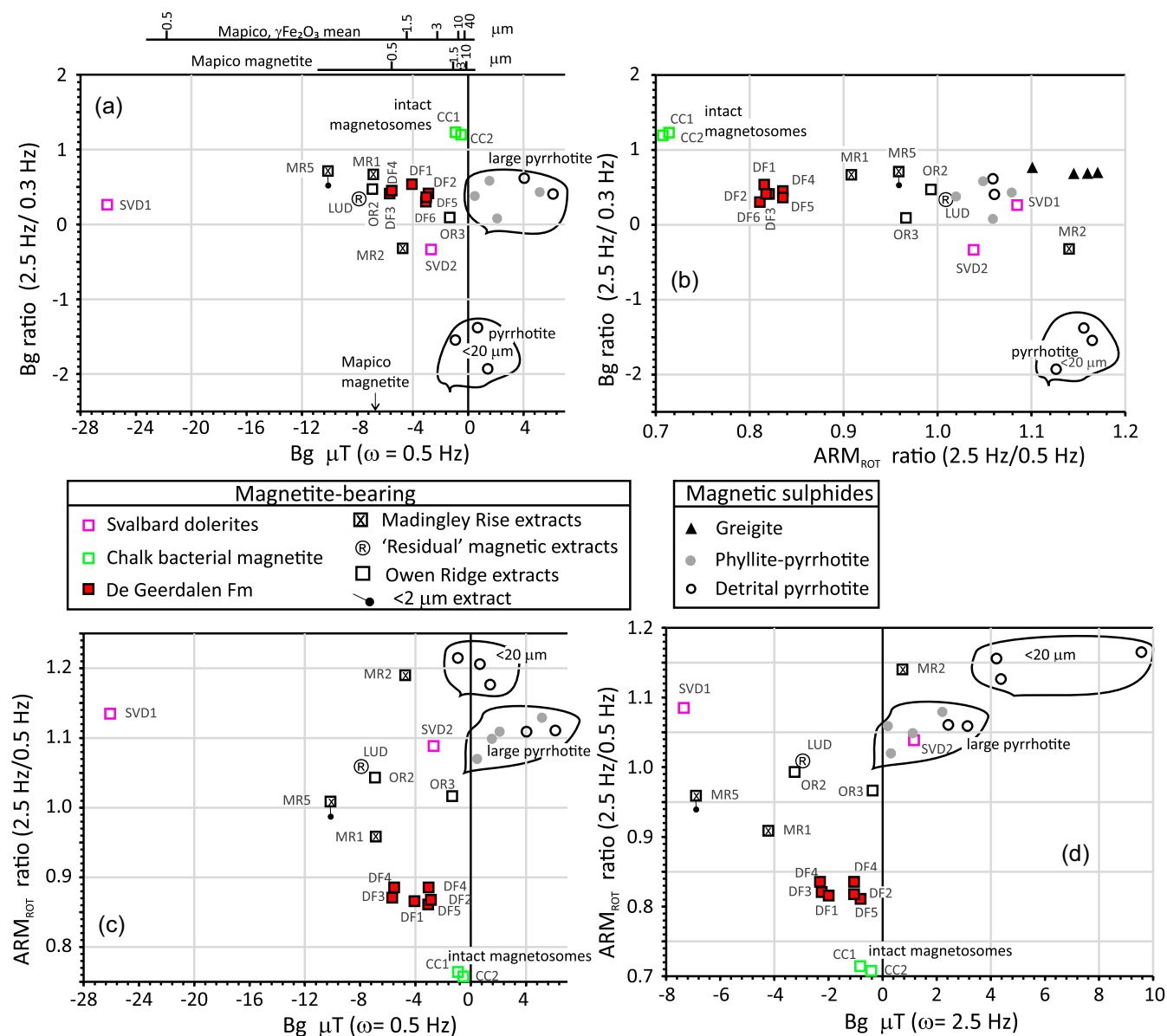


Figure 13. Biplots of Bg and ARM_{ROT} ratios illustrating possible visualization of mineral magnetic discrimination. In (a) at top are shown two possible scales of Bg conversion from the high spin rate data sets (sized and crushed magnetite) of Potter & Stephenson (1986)—scale in microns. The lower micron scale is using the Mapico magnetite (Tables 2 and 3) with Bg value of -8 mT (at $\omega T_D = 1.05$ revolutions), which gives a high to low spin Bg conversion factor of -0.022 . The upper micron scale is using $\gamma\text{Fe}_2\text{O}_3$ (GF01, TDK type D; Tables 2 and 3), which gives a conversion factor of -0.089 . The magnetite-bearing greigite samples plot-off to the left of the graph in (a), (c) and (d). The diagenetic greigite samples plot-off to the left of the graph in (a), (c) and (d).

may be related to the model of magnetization in elongate particles (i.e. equivalent to magnetosome strings) proposed by Potter & Stephenson (2006).

It is challenging to compare the Bg values at high ω with those at low ω . Two ways to approximately cross calibrate these, are to use the Bg for synthetic Mapico magnetite and $\gamma\text{Fe}_2\text{O}_3$ which have been measured at both low and high spin rates (Tables 2 and 3). Using either the Mapico magnetite or mean of Mapico + $\gamma\text{Fe}_2\text{O}_3$ gives two possible conversion factors which allows the Bg to grain size data of Potter & Stephenson (1986) to be mapped into the low spin rate data here (scales in top Fig. 13a). It is feasible, that excluding the Chalk samples, the remaining magnetite-bearing samples show differing Bg values corresponding to the particles size changes suggested by Potter & Stephenson (1986), since samples MR5, MR4 have

the larger contribution from the finest particle sizes (i.e. SD magnetofossils largely not in chains) in the magnetic extracts (Fig. 13a). Perhaps the particle size, d (in μm) dependency of $d \approx 100/\text{Bg}$ (Potter & Stephenson 1986) has compressed much of the apparent grain size variation in our sample set into a range in Bg of ca. $0\text{--}10$ μT at 0.5 Hz [rps] (Fig. 13a). An alternative possibility is that the larger Bg values for the crushed samples of Potter & Stephenson (1986) are related to stress, which can impact coercivity, something clearly expressed in hysteresis data, which strongly modifies the coercivity relationship to grain size (Tauxe *et al.* 2002). Like hysteresis data sets, we speculate that the presence of dislocations allows additional pinning of domain wall motions and so may enhance the irreversible flip-mechanism which is responsible for RRM acquisition. It seems reasonable that during crushing, dislocation density may increase

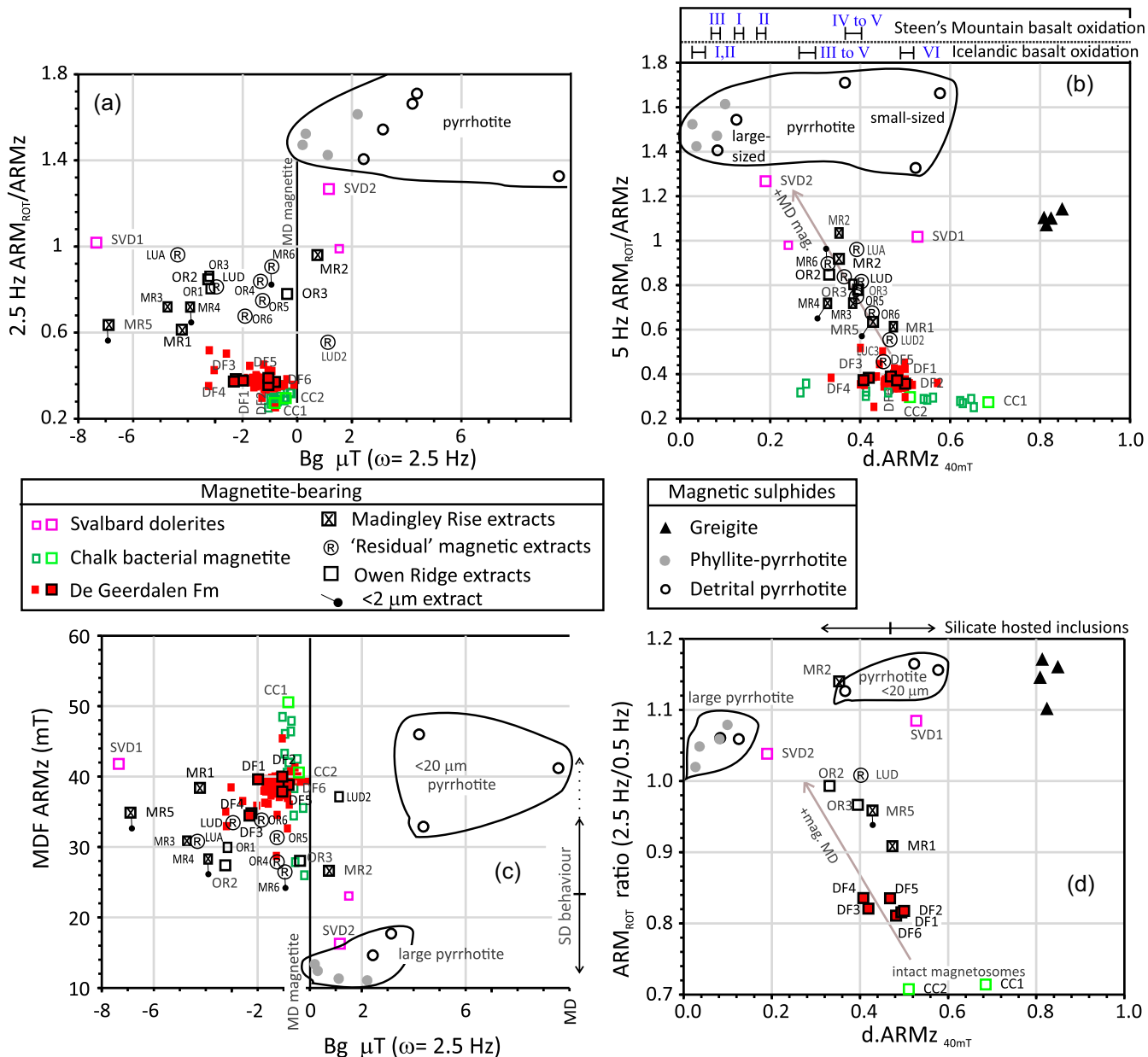


Figure 14. Biplots of RRM, ARMz and demagnetization stability, illustrating possible visualization of mineral magnetic discrimination. In (b) and (c) $d.ARM_z_{40mT}$ is the proportion of the initial ARMz remaining after 40 mT static-axis demagnetization. Regions on the plots for pyrrhotite are loosely defined with a ‘bag’, and the $B_g = 0$ line indicates truly MD magnetite in (a) and (c). Those marked as ‘residual’ contain a residual magnetic assemblage after extensive diagenetic dissolution (samples LUA, LUD, LUD2, LUD3, OR4, OR5, OR6, MR6; Table 4). Various additional unlabelled samples are shown from the Chalk and De Geerdalen Fm sample sets (see Supporting Information data sets). (b) Top scales show the $d.ARM_z_{40mT}$ values for the petrological oxidation states I to VI (Watkins & Haggerty 1967) of basalts from the Steen’s Mountain and Icelandic basalts (from Dunlop 1983). (c) Arrows on right show the mean (the tick) and standard deviation (1σ) range of the MDF of ARMz for basic igneous rock classed as single domain (SD) type by Dunlop (1983) with the dotted arrow showing the maximum MDF in this class. Dunlop’s (1983) MD-type mean and 1σ range falls below 10 mT (so off the graph). (d) Top arrow is the mean (tick) and range of $d.ARM_z_{40mT}$ from Fe-oxides inclusions in silicates (Hounslow & Morton 2004) for nine UK basement complexes (all discrete Fe-oxides outside silicates removed). The greigite samples plot off the graphs to the left in (a) and (c).

in smaller particles, so increasing B_g . Alternatively, the likely particle interactions present in both our magnetic extract samples, and those of Potter & Stephenson (1986) may modify this behaviour—the RRM response to magnetic interactions needs further work to evaluate this.

Excluding the Chalk samples, magnetite-bearing samples show broadly similar declines in B_g from ω from 0.3 to 2.5 Hz [rps], which can be expressed as the B_g ratio at $\omega\{2.5/0.3\}$ —with samples

clustered in the numerical range *ca.* 0 to 0.7 for this B_g ratio (Figs 13a and b). The ratio of the ARM_{rot} for $\omega\{2.5/0.5\}$ shows a better discrimination of these samples (Figs 13c, d and 14d), which expresses the decline in ARM_{rot} with ω . The two dolerite samples (SVD1 and SVD2) show very different RRM behaviour, which is rooted in the differing stability of the natural remanence of the Spitsbergen dolerites which varies much, with some showing MDF of NRM <10 mT, with others up to 40 mT (Halvorsen 1973). This

is reflected in the ARMz stability of SVD1 and SVD2 which are 42 and 16 mT, respectively, with SVD2 showing behaviour closer to MD-like titanomagnetite with small Bg values and low ARMz stability and low MDF of RRM at 0.5 Hz [rps] (Figs 12a, 14c and d). This variability is rooted in the variable oxidation of titanomagnetite in igneous rocks, which impacts ARMz stability (Dunlop 1983; Figs 14b and c). The larger ARMz stability in SVD1 is probably from nanoscale subdivision of the titanomagnetite due to exsolution (cf. Harrison *et al.* 2002) and titanomagnetite oxidation. This is probably responsible for the large Bg value ($-26 \mu\text{T}$) for SVD1 at 0.5 Hz [rps] (Fig. 13a). Sample SVD2 shows similar changes in RRM with ω , to basalt sample F37B-1a studied by Edwards (1982b) derived from R.L. Wilson's samples. All these share a transition into positive RRM values at $\omega T_D > 3$ revolutions (Fig. 4c). Edward's sample F37B-1a had a Bc of 18 mT and *Mrs/Ms* of 0.13 (Edwards 1982a), which places F37B-1a close to the MD-magnetite field using the squareness versus Bc plot of Tauxe *et al.* (2002). Perhaps this positive RRM at larger ωT_D represents the RRM response at the border towards truly MD magnetite, but with a small contribution from SD-like material. Truly MD-behaviour (with zero Bg) is shown by Edwards basalt sample D264-26 (Table 3). Hence, increases in ARM_{ROT} for $\omega\{2.5/0.5\}$ and $\text{ARM}_{\text{ROT}}/\text{ARMz}$ seem to express change towards a more MD state for magnetite-samples, from non-interacting SD-state in the Chalk samples (arrows in Figs 14b and d). Overall, comparing our data set to those of basic igneous rocks, not surprisingly shows that the extracts and sediment sample sets fall into regions corresponding to the most oxidized and most stable SD-like behaviour seen in basic igneous rocks (top scale in Fig. 14b, arrows in Fig. 14c). Our data do not therefore provide much in the way of characterization of the RRM behaviour of low to mid oxidation status basic igneous rocks as characterized by Dunlop (1983)—other than sample SVD2.

Those magnetic extracts corresponding to residual Fe-oxide assemblages, broadly fall into similar intervals as other extracts (Figs 14a–c). This broadly corresponds with observations of silicate hosted inclusions which have similar chemistry and microstructural characteristics to discrete Fe-oxides (Feinberg *et al.* 2005, 2006). This is also displayed in the Fe-oxide inclusion-only ARM data of Hounslow & Morton (2004) from UK basement complexes which show a similar range in $d.\text{ARM}_{40\text{mT}}$ to the samples here (arrows at top in Fig. 14d). The De Geerdalen Formation samples are remarkably well clustered considering the range of locations and lithology types that occur in these samples (Figs 13 and 14). In addition their properties do not overlap those of the magnetic extracts (Figs 14a, c and d), but do overlap with the range of $d.\text{ARM}_{40\text{mT}}$ seen in silicate hosted inclusions. Hence, presumably these contain more SD-like magnetite which is intermediate towards the Chalk samples, with a larger MDF of ARMz (Fig. 14c). Although magnetic extracts have not been performed on these samples, it seems highly unlikely they contain magnetofossils, due to the rather extensive silicate and carbonate diagenesis (Mørk 2013), suggesting magnetite inclusions in silicates likely make significant contributions.

7 CONCLUSIONS

Using rotation rates of 0.26–3 Hz [rps] there is the possibility for routine magnetic mineral characterization using RRM and rotational anhysteretic magnetization (ARM_{ROT}). Characterization is best done using either: (1) normalized ω —RRM curve characteristics (or ω —Bg, ω — ARM_{ROT} curves), This approach allows more effective characterization of the mineralogical behaviour, rather than relying on single spin rate-derived values of Bg, RRM or ARM_{ROT}

or (2) parametrization of the variations using values at selected rotation rates (or better at fixed ωT_D values). The later approach is likely more widely accessible if rotation rates cannot be continuously varied in equipment available. Optimization of the AF field hold time to achieve full rotational initialization of RRM will improve consistency, especially so for investigating greigite (and other strongly anisotropic samples), which shows large changes in RRM and ARM_{ROT} at rotation angles below the initialization threshold, caused by anisotropy.

Static AF demagnetization of the RRM, for stability tests, is best achieved by demagnetization of both $+\omega$ and $-\omega$ RRM's which allows removal of gyroremanence acquired along the axis of demagnetization. A simpler approach free from this problem is to characterize stability using RRM acquisition with increasing AF field—this is probably best standardized at $\omega T_D = 0.4$ revolutions, since RRM stability varies with rotation rate, and RRM is maximized at $\omega T_D = 0.4$. This allows RRM stability to be parametrized even in samples acquiring a weak RRM.

The sized pyrrhotite and pyrrhotite bearing phyllite samples show largely positive RRM, in contrast to negative RRM largely acquired by test samples of magnetite and greigite. This and the smaller variation of RRM and ARM_{ROT} with rotation rate are a simple effective tool for detecting pyrrhotite. The median destructive field of RRM produced by pyrrhotite (including large grains) is comparable to greigite and larger than most test samples of magnetite. Samples of diagenetic greigite display large negative Bg values and a stronger variation of RRM and ARM_{ROT} with spin rate. The large Bg values carried by diagenetic greigite are a simple and easy way to identify it, but additionally diagnostic are the ratio of ARM_{ROT} at $\omega\{2.5/0.5\}$ and MDF of a conventional static ARM. RRM distinction of greigite magnetofossils from magnetite magnetofossils needs more evaluation, but utilizing ω - ARM_{ROT} changes or ARM_{ROT} stability may be diagnostic.

The set of natural magnetite-bearing test samples shows that Bg is not simply related to grain size as thought previously, but non-interacting SD magnetite in magnetofossils have very small Bg and little variation with ω . A small Bg value concurs with studies by Chen (2014) measured at high spin rates on magnetite magnetosomes. The ratio of ARM_{ROT} at $\omega\{2.5/0.5\}$ may be a better tool for particle size characterization of magnetite. For magnetite, the Bg parameter may also be strongly impacted by presence of dislocations, or perhaps interaction-related controls—features that need further study. The prior extensive study of RRM on sized and crushed magnetite by Potter & Stephenson (1986), may have been impacted by particle size related dislocation density in the magnetite samples, which may have enhanced the Bg variation with grain size. The great advantage of using RRM characteristics for magnetic mineral identification is the RRM properties are carried by the hardest coercivity grains most relevant to understanding stable palaeomagnetic signals.

ACKNOWLEDGMENTS

Paul Montgomery helped collect the Chalk samples, and Gareth Lord some of the Svalbard samples. Isaac Hilburn helped unravelling some complexities of the RAPID software.

DATA AVAILABILITY

All data are incorporated into the article and its online supplementary material.

AUTHOR CONTRIBUTION

MWH, VK and C-S.H processed the data. MWH analysed the magnetic results. All contributed to writing of the paper.

REFERENCES

- Chen, A.P., 2014. Rock magnetic properties of uncultivated magnetotactic bacteria and paleo-redox changes across the Paleocene-Eocene boundary, *Unpublished PhD thesis*, Macquarie Univ, New Jersey Coastal Plain.
- Cisowski, S., 1981. Interacting vs. non-interacting single domain behavior in natural and synthetic samples, *Phys. Earth planet. Inter.*, **26**, 56–62.
- Dunlop, D.J., 1983. Determination of domain structure in igneous rocks by alternating field and other methods, *Earth planet. Sci. Lett.*, **63**, 353–367.
- Edwards, J., 1980a. An experiment relating to rotational remanent magnetization and frequency of demagnetizing field, *Geophys. J. Int.*, **60**, 283–288.
- Edwards, J., 1980b. Comparisons between the generation and properties of rotational remanent magnetization and anhysteretic remanent magnetization, *Geophys. J. Int.*, **62**, 379–392.
- Edwards, J., 1982a. Gyroremanent magnetization produced by specimen rotation between successive alternating field treatments, *Geophys. J. Int.*, **71**, 199–214.
- Edwards, J., 1982b. Studies of partial rotational remanent magnetization and rotational remanent magnetization at slow speeds of rotation, *Geophys. J. Int.*, **68**, 609–624.
- Edwards, J., 1984. Partial anhysteretic remanent magnetizations produced in rotating samples, and comparisons with corresponding rotational remanent magnetizations, *Geophys. J. Int.*, **77**, 619–637.
- Edwards, J. & Desta, M., 1989. Static alternating field demagnetizations of anhysteretic and rotational remanent magnetizations in rocks and synthesized samples, *Geophys. J. Int.*, **99**, 739–748.
- Feinberg, J.M., Harrison, R.J., Kasama, T., Dunin-Borkowski, R.E., Scott, G.R. & Renne, P.R., 2006. Effects of internal mineral structures on the magnetic remanence of silicate-hosted titanomagnetite inclusions: an electron holography study, *J. geophys. Res.*, **111**(B12), doi:10.1029/2006JB004498.
- Feinberg, J.M., Scott, G.R., Renne, P.R. & Wenk, H.R., 2005. Exsolved magnetite inclusions in silicates: features determining their remanence behavior, *Geology*, **33**, 513–516.
- Finn, D. & Coe, R., 2020. Consequences of switching field angular dependence for applications of anhysteretic remanent magnetization, *Phys. Earth planet. Inter.*, **305**, doi:10.1016/j.pepi.2020.106507.
- Franke, C., von Dobeneck, T., Drury, M.R., Meeldijk, J.D. & Dekkers, M.J., 2007. Magnetic petrology of equatorial Atlantic sediments: electron microscopy results and their implications for environmental magnetic interpretation, *Paleoceanogr. Paleoclimatol.*, **22**(4), doi:10.1029/2007PA001442.
- Gayer, R.A., Gee, D.G., Harland, W.B., Miller, J.A., Spall, H.R., Wallis, R.H. & Winsnes, T.S., 1966. Radiometric age determinations on rocks from Spitsbergen, *Norsk Polarinst. Skrifter*, Research report, Series: Skrifter;137, Norsk Polarinstittutt.
- Haile, B.G., Klausen, T.G., Czarniecka, U., Xi, K., Jähren, J. & Hellevang, H., 2018. How are diagenesis and reservoir quality linked to depositional facies? A deltaic succession, Edgeøya, Svalbard, *Mar. Petrol. Geol.*, **92**, 519–546.
- Hailwood, E.A. & Molyneux, L., 1974. Anhysteretic remanent magnetization due to asymmetrical alternating fields, *Geophys. J. Int.*, **39**, 421–434.
- Halvorsen, E., 1973. Demagnetization studies of the late Mesozoic dolerites from the Isfjorden area, Spitsbergen, *Arbok - Norsk Polarinstittutt*, **63**, 17–29.
- Harrison, R.J., Dunin-Borkowski, R.E. & Putnis, A., 2002. Direct imaging of nanoscale magnetic interactions in minerals, *Proc. Natl. Acad. Sci.*, **99**, 16 556–16561.
- Hornig, C.S., 2018. Unusual magnetic properties of sedimentary pyrrhotite in methane seepage sediments: comparison with metamorphic pyrrhotite and sedimentary greigite, *J. geophys. Res.*, **123**, 4601–4617.
- Hornig, C.S., Huh, C.A., Chen, K.H., Lin, C.H., Shea, K.S. & Hsiung, K.H., 2012. Pyrrhotite as a tracer for denudation of the Taiwan orogen, *Geochem., Geophys., Geosyst.*, **13**(8), doi:10.1029/2012GC004195.
- Hornig, C.S. & Roberts, A.P., 2006. Authigenic or detrital origin of pyrrhotite in sediments? Resolving a paleomagnetic conundrum, *Earth planet. Sci. Lett.*, **241**, 750–762.
- Hornig, C.S., Torii, M., Shea, K.S. & Kao, S.J., 1998. Inconsistent magnetic polarities between greigite- and pyrrhotite/magnetite-bearing marine sediments from the Tsailiao-chi section, southwestern Taiwan, *Earth planet. Sci. Lett.*, **164**, 467–481.
- Hounslow, M.W., 2019. GM4Edit (v.5.6) - a windows program to manage, plot, export and manipulate palaeomagnetic magnetometer data sets, doi:10.13140/RG.2.2.31877.91361/1.
- Hounslow, M.W., 1996. Ferrimagnetic Cr and Mn spinels in sediments: residual magnetic minerals after diagenetic dissolution, *Geophys. Res. Lett.*, **23**, 2823–2826.
- Hounslow, M.W., Hu, M., Mørk, A., Vigran, J.O., Weitschat, W. & Orchard, M.J., 2007. Magneto-biostratigraphy of the Middle to Upper Triassic transition, central Spitsbergen, arctic Norway, *J. Geol. Soc.*, **164**, 581–597.
- Hounslow, M.W. & Maher, B.A., 1996. Quantitative extraction and analysis of carriers of magnetization in sediments, *Geophys. J. Int.*, **124**, 57–74.
- Hounslow, M.W. & Maher, B.A., 1999. Laboratory procedures for quantitative extraction and analysis of magnetic minerals from sediments, in *Environmental Magnetism, A Practical Guide*, Vol. 6, pp. 139–164, eds Oldfield, F. & Smith, J.P., Technical Guide, Quaternary Research Association.
- Hounslow, M.W., Maher, B.A. & Thistlewood, L., 1995. Magnetic mineralogy of sandstones from the Lunde Formation (late Triassic), northern North Sea, UK: origin of the palaeomagnetic signal, in *Palaeomagnetic Applications in Hydrocarbon Exploration and Production*, Vol. 98, pp. 119–147, eds Turner, P. & Turner, A., Geological Society, London, Special Publications.
- Hounslow, M.W. & Morton, A.C., 2004. Evaluation of sediment provenance using magnetic mineral inclusions in clastic silicates: comparison with heavy mineral analysis, *Sediment. Geol.*, **171**, 13–36.
- Hounslow, M.W., Samuel, E., Harris, Karloukovski, V. & Mørk, A., 2022. Geomagnetic polarity and carbon isotopic stratigraphic assessment of the Carnian-Norian boundary on Hopen and Wilhelmøya (Svalbard), *Norveg. J. Geol.*, **102**, doi:10.17850/njg102-1-4.
- Hu, S., Appel, E., Hoffmann, V., Schmahl, W.W. & Wang, S., 1998. Gyromagnetic remanence acquired by greigite (Fe₃S₄) during static three-axis alternating field demagnetization, *Geophys. J. Int.*, **134**, 831–842.
- Hu, S., Stephenson, A. & Appel, E., 2002. A study of gyroremanent magnetisation (GRM) and rotational remanent magnetisation (RRM) carried by greigite from lake sediments, *Geophys. J. Int.*, **151**, 469–474.
- Jiang, W.T., Hornig, C.S., Roberts, A.P. & Peacor, D.R., 2001. Contradictory magnetic polarities in sediments and variable timing of neof ormation of authigenic greigite, *Earth planet. Sci. Lett.*, **193**, 1–12.
- Kirschvink, J.L., Kopp, R.E., Raub, T.D., Baumgartner, C.T. & Holt, J.W., 2008. Rapid, precise, and high-sensitivity acquisition of paleomagnetic and rock-magnetic data: development of a low-noise automatic sample changing system for superconducting rock magnetometers, *Geochem., Geophys., Geosyst.*, **9**(5), doi:10.1029/2007GC001856.
- Kopp, R.E. & Kirschvink, J.L., 2008. The identification and biogeochemical interpretation of fossil magnetotactic bacteria, *Earth-Sci. Rev.*, **86**, 42–61.
- Krumsiek, K., Nagel, J. & Nairn, A.E.M., 1968. Record of palaeomagnetic measurements on some igneous rocks from the Isfjorden region, Spitsbergen, *Norsk Polarinstittutt Årbok*, **1966**, 76–83.
- Lesniak, B., Koulialias, D., Charilaou, M., Weidler, P.G., Rhodes, J.M., Macdonald, J.E. & Gehring, A.U., 2021. Polycrystalline texture causes magnetic instability in greigite, *Scient. Rep.*, **11**, 1–10.
- Madsen, K.N., 2004. Angular dependence of the switching field and implications for gyromagnetic remanent magnetization in three-axis alternating-field demagnetization, *Geophys. J. Int.*, **157**, 1007–1016.
- Madsen, K.N., 2003. A reversed gyromagnetic effect in chromium dioxide particles, *J. Magn. Magn. Mater.*, **260**, 131–140.

- Maher, B.A. & Hallam, D.F., 2005. Magnetic carriers and remanence mechanisms in magnetite-poor sediments of Pleistocene age, southern North Sea margin, *J. Quater. Sci.*, **20**, 79–94.
- Maher, B.A. & Hounslow, M.W., 1999. The significance of magnetotactic bacteria for the palaeomagnetic and rock magnetic record of Quaternary sediments and soils, in *Palaeomagnetism and Diagenesis in Sediments*, Vol. **151**, pp. 43–46, eds Tarling, D.H. & Turner, P., Geological Society, London, Special Publications.
- Mahon, S.W. & Stephenson, A., 1997. Rotational remanent magnetization (RRM) and its high temporal and thermal stability, *Geophys. J. Int.*, **130**, 383–389.
- Montgomery, P., Hailwood, E.A., Gale, A.S. & Burnett, J.A., 1998. The magnetostratigraphy of Coniacian-Late Campanian chalk sequences in southern England, *Earth planet. Sci. Lett.*, **156**, 209–224.
- Mork, M.B.E., 2013. Diagenesis and quartz cement distribution of low-permeability Upper Triassic–Middle Jurassic reservoir sandstones, Longyearbyen CO₂ lab well site in Svalbard, Norway, *AAPG Bull.*, **97**, 577–596.
- Nejbert, K., Krajewski, K.P., Dubinska, E. & Pecskey, Z., 2011. Dolerites of Svalbard, north-west Barents Sea Shelf: age, tectonic setting and significance for geotectonic interpretation of the High-Arctic Large Igneous Province, *Polar Res.*, **30**, doi:10.3402/polar.v30i0.7306.
- Noel, M., 1988. Some observations of the gyroremanent magnetization acquired by rocks in a rotating magnetic field, *Geophys. J. Int.*, **92**, 107–110.
- Peters, C. & Thompson, R., 1998. Magnetic identification of selected natural iron oxides and sulphides, *J. Magn. Magn. Mater.*, **183**, 365–374.
- Potter, D.K., 2004. A comparison of anisotropy of magnetic remanence methods—a user's guide for application to palaeomagnetism and magnetic fabric studies, in *Magnetic Fabric: Methods and Applications*, Vol. **238**, pp. 21–35, eds Martin-Hernandez, F., Luneburg, C.M., Aubourg, C. & Jackson, M., Geological Society, London, Special Publications.
- Potter, D.K. & Stephenson, A., 1986. The detection of fine particles of magnetite using anhysteretic and rotational remanent magnetizations, *Geophys. J. Int.*, **87**, 569–582.
- Potter, D.K. & Stephenson, A., 2006. The stable orientations of the net magnetic moment within single-domain particles: experimental evidence for a range of stable states and implications for rock magnetism and palaeomagnetism, *Phys. Earth planet. Inter.*, **154**, 337–349.
- Reinholdsson, M., Snowball, I., Zillén, L., Lenz, C. & Conley, D.J., 2013. Magnetic enhancement of Baltic Sea sapropels by greigite magnetofossils, *Earth planet. Sci. Lett.*, **366**, 137–150.
- Roberts, A.P., 2015. Magnetic mineral diagenesis, *Earth-Sci. Rev.*, **151**, 1–47.
- Roperch, P. & Taylor, G.K., 1986. The importance of gyromagnetic remanence in alternating field demagnetization. Some new data and experiments on GRM and RRM, *Geophys. J. Int.*, **87**, 949–965.
- Slotznick, S.P., Winston, D., Webb, S.M., Kirschvink, J.L. & Fischer, W.W., 2016. Iron mineralogy and redox conditions during deposition of the mid-Proterozoic Appekunny Formation, Belt Supergroup, Glacier National Park, in *Belt Basin: Window to Mesoproterozoic Earth*, Vol. **522**, pp. 1–22, eds MacLean, J.S. & Sears, J.W., Society of America Special Paper.
- Snowball, I.F., 1997a. Gyromagnetic magnetization and the magnetic properties of greigite-bearing clays in southern Sweden, *Geophys. J. Int.*, **129**, 624–636.
- Snowball, I.F., 1997b. The detection of single-domain greigite (Fe₃S₄) using rotational remanent magnetization (RRM) and the effective gyro field (Bg): mineral magnetic and palaeomagnetic applications, *Geophys. J. Int.*, **130**, 704–716.
- Stephenson, A., 1981. Gyromagnetic remanence and anisotropy in single domain particles, rocks and magnetic recording tape, *Philos. Mag. B*, **44**, 635–664.
- Stephenson, A., 1980. Rotational remanent magnetization and the torque exerted on a rotating rock in an alternating magnetic field, *Geophys. J. Int.*, **62**, 113–132.
- Stephenson, A., 1983. Changes in direction of the remanence of rocks produced by stationary alternating field demagnetization, *Geophys. J. Int.*, **73** (1), 213–239.
- Stephenson, A., 1985. The angular dependence of rotational and anhysteretic remanent magnetizations in rotating rock samples, *Geophys. J. Int.*, **83**, 787–796.
- Stephenson, A., 1988. Gyromagnetic remanence produced by rotation of magnetite and maghemite particles in a slowly reducing direct field, *J. Magn. Magn. Mater.*, **71**, 179–185.
- Stephenson, A. & Molyneux, L., 1987. The rapid determination of rotational remanent magnetization and the effective field which produces it, *Geophys. J. Int.*, **90**, 467–471.
- Stephenson, A. & Snowball, I.F., 2001. A large gyromagnetic effect in greigite, *Geophys. J. Int.*, **145**, 570–575.
- Stephenson, R.W., 1976. A study of rotational remanent magnetization, *Geophys. J. Int.*, **47**, 363–373.
- Tauxe, L., Bertram, H.N. & Seberino, C., 2002. Physical interpretation of hysteresis loops: micromagnetic modeling of fine particle magnetite, *Geochem., Geophys., Geosyst.*, **3**(10), doi:10.1029/2001GC000241.
- Thomson, G.F., 1990. The anomalous demagnetization of pyrrhotite, *Geophys. J. Int.*, **103**, 425–430.
- Vincenz, S.A., Jeleńska, M., Aiiinhsazian, K. & Birkenmajer, K., 1984. Palaeomagnetism of some late Mesozoic dolerite sills of east central Spitsbergen, Svalbard Archipelago, *Geophys. J. Int.*, **78**, 751–773.
- Watkins, N.D. & Haggerty, S.E., 1967. Primary oxidation variation and petrogenesis in a single lava, *Contrib. Mineral. Petrol.*, **15**, 251–271.
- West, G.F. & Dunlop, D.J., 1971. An improved ballistic magnetometer for rock magnetic experiments, *J. Phys. E: Scient. Instrum.*, **4**, 37, doi:10.1088/0022-3735/4/1/009.
- Wilson, R.L. & Lomax, R., 1972. Magnetic remanence related to slow rotation of ferromagnetic material in alternating magnetic fields, *Geophys. J. Int.*, **30**, 295–303.

SUPPORTING INFORMATION

Supplementary data are available at [GJI](https://doi.org/10.1017/gji.2024.11) online.

Figure S1. Representative XRD data for the sized natural pyrrhotite samples (5–10 μm and 38–63 μm, respectively) separated from river sediment by using magnetic extraction.

Figure S2. Magnetic hysteresis loops after slope correction for a) (top) pyrrhotite-bearing and b) (bottom) greigite-bearing test samples. Hysteresis parameters Ms, Mrs, Bc, and Bcr are shown in Table S1.

Figure S3. Magnetofossil morphology and sizes in the E_{mpt} extract from Chalk sample CC9b.

Figure S4. A) The magnetofossil size and aspect ratio (n = 312) from Upper Chalk sample CC9b plotted onto the domain state diagram for magnetite. SD = single domain, TD = two domain, SP = superparamagnetic. B) Transmission electron micrograph of magnetofossils of various morphologies in the CC9b E_{mpt} magnetic extract.

Figure S5. X-ray diffraction data for the magnetic extracts (b-f), and two example ones from the Chalk (a).

Figure S6. Low temperature magnetic susceptibility data for the magnetic extract samples (prior to the magnetic extraction, but after carbonate removal).

Figure S7. Thermal demagnetisation of the normalised ARMz (J/J₀) in whole-rock specimens representative of the Lunde extracts.

Figure S8. Thermal demagnetisation of a three component IRM in samples representative of the Lunde magnetic extracts (soft = 0–0.1 T, medium = 0.1–0.3 T; Hard = 0.3–1 T coercivity fractions).

Figure S9. Typical features of the magnetic extract test samples.

Figure S10. The standard deviation of the raw measured moments (MSD) along the Z-axis (i.e., that which the RRM and ARMz are acquired along) versus the magnitude of the measured moment (after removal of holder+ rod moment).

Figure S11. The standard deviation (RSD) of the limited number of RRM repeats.

Figure S12. Standard deviation of the sample remanence after being subjected to AF demagnetisation at 150 mT along the Z-axis (ZSD), versus the RRM moment acquired at 100 mT.

Figure S13. The relationship of the transverse static ARM (ARM_{trans}) to the ARM_{ROT} values at rotation rates of 0.5 revs^{-1} (panel D) and 2.5 Hz [rps] (panels A, B and C; $T_H = 92 \text{ ms}$).

Figure S14. Data for the RRM acquired under zero DC bias and that acquired during a DC bias field of 100 mT (i.e. RRM_{100}) at $\omega = 2.5 \text{ Hz}$ [rps] (A, B, C) and with respect to rotation rate in D and E.

Figure S15. Data for the RRM of pyrrhotite and greigite acquired under zero DC bias and that acquired with a DC bias field of 100 mT (RRM_{100}) at rotation rates ω of 0.05 to 3 Hz [rps] (sample codes as in this work, $T_H = 92 \text{ ms}$).

Figure S16. Variation of RRM and ARM_{ROT} acquisition with AF field intensity for four test samples.

Figure S17. Variation of normalised RRM, ARM_{ROT} and B_g with respect to rotation rates.

Figure S18. The percentage of RRM and ARM_{ROT} acquired between 40-100mT with respect to the rotation rate.

Figure S19. The variation of B_g with rotation rate for the three tested values of peak AF hold times.

Figure S20. Data for RRM and RRM_{100} with respect to rotation rate for the three peak AF hold times tested.

Figure S21. The data for the test of the T_H and field frequency. The x-axis is the parameter D set in the RAPID software.

Table S1. Hysteresis parameters (after paramagnetic slope correction) for the pyrrhotite-bearing (PY6-PY9) and greigite-bearing (GR1-GR4) test samples.

Table S2. Summary magnetic and magnetic extraction data for the magnetic extracts.

Table S3. Summary mineralogical data for the magnetic extracts, largely based on semi-quantitative XRD, using the method detailed in Hounslow & Maher (1999).

Table S4. Shows the relationships of sample codes used here and in prior publications (Hounslow *et al.* 1995; Hounslow 1996; Hounslow & Maher, 1996, 1999) about these extracts.

Please note: Oxford University Press is not responsible for the content or functionality of any supporting materials supplied by the authors. Any queries (other than missing material) should be directed to the corresponding author for the paper.